

# Multiple fluid flow events from salt-related rifting to basin inversion (Upper Pedraforca thrust sheet, SE Pyrenees)

David Cruset<sup>1,2</sup>  | Jaume Vergés<sup>1</sup>  | Antonio Benedicto<sup>3</sup> |  
 Enrique Gomez-Rivas<sup>2</sup>  | Irene Cantarero<sup>2</sup>  | Cédric M. John<sup>4</sup>  | Anna Travé<sup>2</sup> 

<sup>1</sup>Group of Dynamics of the Lithosphere (GDL), Geosciences Barcelona (GEO3BCN-CSIC), Barcelona, Spain

<sup>2</sup>Departament de Mineralogia, Petrologia i Geologia Aplicada, Facultat de Ciències de la Terra, Universitat de Barcelona (UB), Barcelona, Spain

<sup>3</sup>UMR Geops, Université Paris Sud, Orsay, France

<sup>4</sup>Department of Earth Science and Engineering and Qatar Carbonate and Carbon Storage Research Center, Imperial College London, London, UK

## Correspondence

Jaume Vergés, Group of Dynamics of the Lithosphere (GDL), Geosciences Barcelona (GEO3BCN-CSIC), Lluís Solé i Sabarís s/n, 08028 Barcelona, Spain.  
 Email: jverges@gco3bcn.csic.es

## Funding information

DGICYT Spanish Project PGC2018-093903-B-C22 Ministerio de Ciencia, Innovación y Universidades/Agencia Estatal de Investigación/Fondo Europeo de Desarrollo Regional, Unión Europea; SUBTETIS, Grant/Award Number: PIE-CSIC-201830E039; ALORBE, Grant/Award Number: PIE-CSIC-202030E310; Grup Consolidat de Recerca "Geologia Sedimentària", Grant/Award Number: 2017SGR-824; Generalitat de Catalunya, Grant/Award Number: AGAUR 2017SGR-847; "Ramón y Cajal" fellowship, Grant/Award Number: RYC2018-026335-I; FEDER-UE, Grant/Award Number: Ref. CSIC08-4E-001

## Abstract

Fluid systems in inverted rifted margins are challenging to interpret because fractures formed before compression were often reactivated acting as fluid pathways as new ones formed. Deciphering the fracture and fluid flow history in such complex settings has key implications for the prediction of the distribution of mineral resources. As an example, we reconstruct the fluid flow evolution of a portion of the inverted Pyrenean rift, the Upper Pedraforca thrust sheet, from the Mesozoic extension to the Alpine orogeny. We combine structural analysis and petrographic, geochemical and geochronological data obtained from 87 samples of fracture-filling carbonate cements. During the Late Jurassic-Early Cretaceous, low-temperature seawater produced dolomitization of Jurassic and Lower Cretaceous limestones in an extensional setting. During the Early Cretaceous salt-related extension, formation waters, probably evolved seawater or fluids that interacted with Triassic evaporites, at temperatures from 125 to 149°C migrated through fractures. The formation of breccias within post-salt rocks in primary weld zones facilitated the upward migration of formation waters that interacted with pre-salt rocks with high <sup>87</sup>Sr/<sup>86</sup>Sr ratios. Formation waters at temperatures of 80°C migrated during the emplacement of the Upper Pedraforca thrust sheet in the Late Cretaceous-Palaeocene. These fluids interacted with Upper Cretaceous Carbonates and/or Triassic evaporites. In contrast, the influence of meteoric fluids increased in shallower positions due to the exhumation of the SE Pyrenees during the Eocene-Oligocene. Coevally, hot dolomitizing fluids migrated along diapir walls during the formation of secondary welds. Supergene ores documented in diapiric areas worldwide related to meteoric fluids, and the similar meteoric percolation occurred in the Upper Pedraforca thrust sheet, suggest that supergene mineralization could be found in the Pyrenees. Brecciation of rocks in primary weld zones and evaporite detachments, where mineralization accumulate in fractures from basement-derived fluids, also suggests that similar ores could be found in the Pyrenees.

This is an open access article under the terms of the Creative Commons Attribution License, which permits use, distribution and reproduction in any medium, provided the original work is properly cited.

© 2021 The Authors. *Basin Research* published by International Association of Sedimentologists and European Association of Geoscientists and Engineers and John Wiley & Sons Ltd.

## KEYWORDS

evaporitic detachment, fluid flow history, fracture-filling cements, inversion tectonics, salt-related extension, South Pyrenean thrust sheets

## 1 | INTRODUCTION

Pre-compressive thick evaporite units forming diapirs and/or detachment levels, can strongly control the palaeohydrology of fold and thrust belts and their related foreland basins, because fluids migrate induced by tectonic and topographic gradients in areas adjacent to evaporite bodies or along their boundaries (Crognier et al., 2018; Fischer et al., 2009, 2013; Moragas et al., 2020; Reuning et al., 2009; Smith et al., 2012). Under certain circumstances, geological resources such as hydrocarbons, accumulate below evaporite seals and structural traps (e.g. folds and faults), which form due to salt and gypsum flow during rifting and thrusting (Allen & Allen, 2005; Davison et al., 2000). Other resources, such as metalliferous ore deposits (i.e. Pb-Zn), can be associated with the interaction of fluids with saline bodies (Perona et al., 2018; Rouvier et al., 1985; Sheppard et al., 1996).

Evaporite-bearing basins can be incorporated into compressional belts, reactivating the pre-compressive fracture patterns, thus resulting in complex fracture cross-cutting relationships (e.g. Moragas et al., 2020; Salardon et al., 2017; Smith et al., 2012). As a result, previous traps, formed during pre-compressive stages, can be destroyed or modified, allowing changes in the palaeohydrological system and/or the re-mobilization of trapped fluids in the subsurface (Cooper & Warren, 2010; Roure et al., 2005). Considering the importance of salt-related structures on the development and storage of resources of economic interest, the overarching aim of this study is to characterize the heterogeneity and evolution of fluid systems in sedimentary basins affected by rift-related diapirism, as well as by subsequent inversion during orogenic compression.

There are many examples of fluid systems in rifted margins and fold and thrust belts with resources of economic interest, and where multiple processes of fracturing, fracture reactivation, dolomitization or ore deposit remobilization occurred due to basin inversion or long-lasting tectonic deformation. Some case studies are the External Crystalline Massifs of the Western Alps (Boutoux et al., 2014; Incerpi et al., 2020), the Variscan Belt of Morocco (N'Diaye et al., 2016), the northern Oman Mountains (Fontana et al., 2014; Gomez-Rivas, Bons, et al., 2014), the Ionian and Zagros fold and thrust belts (Sharp et al., 2010; Van Geet et al., 2002) and the Neuquén basin of Argentina (Cobbold et al., 1999; Cruset et al., 2021;

### Highlights

- We decipher the fluid history in a portion of the Mesozoic Pyrenean rift, which was inverted during the Alpine orogeny.
- Hot formation waters migrated along fractures during Early Cretaceous diapirism.
- Formation of primary welds facilitated the migration of high  $^{87}\text{Sr}/^{86}\text{Sr}$  fluids that interacted with pre-salt rocks.
- Formation waters migrated along major thrust faults zones during Cretaceous-Palaeocene and Eocene-Oligocene.
- Meteoric percolation increased during the Paleogene during the exhumation of the SE Pyrenees.

Rodrigues et al., 2009; Weger et al., 2019) among others. Nevertheless, although the evolution of fracture networks and fluid chemistry of these areas are well-characterized, the absolute timing of these processes is not always accurately constrained. Nowadays, relative and absolute time uncertainties can be solved by combining fracture analysis and modern geochemical and geochronological methods applied to porosity-filling minerals (e.g. clumped isotopes thermometry and U-Pb dating of carbonates). This is attested by the increasing number of publications that characterize fluid systems in compressional settings affected by long-lasting deformation and burial (e.g. Al Hajar Mountains of Oman, Hansman et al., 2018; Northwestern Alps, Incerpi et al., 2020; Southern Pyrenees, Cruset, Cantarero, et al., 2020; Hoareau et al., 2021; Paris and South Eastern Basins, Godeau et al., 2018; Mangenot et al., 2018; Pagel et al., 2018).

Here, we focus on the Southern Pyrenees, which have been considered as an excellent natural laboratory to tackle the proposed research question in this contribution, as demonstrated by the large number of publications on fluid flow and geochronology of fracture-filling minerals in the Palaeogene lower thrust sheets published in the last decades (e.g. Banks et al., 1991; Beaudoin et al., 2015; Caja et al., 2006; Crognier et al., 2018; Cruset et al., 2018;

Cruset, Cantarero, et al., 2020; Hoareau et al., 2021; Lacroix et al., 2018; Muñoz-López, Cruset, et al., 2020; Nardini et al., 2019; Rahl et al., 2011; Travé et al., 2007; Trincal et al., 2017). The results of these studies indicate that fluid flow during Pyrenean compression was multiepisodic and report the progressive exhumation of the Pyrenean thrust sheets as well as the influence of the basement lithology, detachment evaporite levels and connate marine fluids trapped within sediments on the fluid composition. However, there is a knowledge gap on the uppermost Late Cretaceous-Palaeocene emplaced thrust sheets, which have undergone post-emplacement deformation by being tectonically transported to the south on top of younger and lower thrust sheets (Burbank, Puigdefàbregas, et al., 1992; Burbank, Vergés, et al., 1992; Cruset, Vergés, et al., 2020; Vergés et al., 2002). As a result, these nappes experienced a more complex and heterogeneous fluid flow and deformation history than their underlying thrust sheets. An example of this is the Upper Pedraforca thrust sheet, the oldest and uppermost structural unit of the SE Pyrenees. This thrust sheet is part of the northernmost preserved portion of the Mesozoic Pyrenean rifted basin affected by diapirism during the Late Jurassic-Early Cretaceous extension, which was, later on, incorporated into the Pyrenean orogen during the Late Cretaceous to Oligocene compression (Cruset, Vergés, et al., 2020; Saura et al., 2016; Vergés, 1993). To decipher the fracture and fluid flow evolution of the Upper Pedraforca thrust sheet, we combine fracture orientation data, petrographic observations and geochemical analyses applied to fracture-filling calcite and dolomite (e.g. REE+Y and Sr, C, O and clumped isotopes) with already published U-Pb ages of the study area (Cruset, Vergés, et al., 2020). The results of this study provide absolute time constraints and knowledge about: (1) how syn-tectonic fluid flow is recorded and distributed in sedimentary basins involved in long-lasting deformation and (2) what the potential impact is of the changes in palaeofluid systems on the development and/or alteration of ore mineralization in diapir structures.

## 2 | GEOLOGICAL SETTING

The Pyrenees (Figure 1a) formed due to the collision between Iberia and Eurasia from the Late Cretaceous to the Miocene, during the Alpine orogeny (Choukroune et al., 1989; Muñoz, 1992, 2002; Roure et al., 1989; Vergés et al., 2002). As a consequence, the Mesozoic northern Iberian rift margin was inverted and thrust southwards above the thrust stack of basement units that form the Pyrenees Axial Zone limited by the North Pyrenean Fault in the north (Figure 1b) (Muñoz, 1992). The South Pyrenean fold and thrust belt consists of a piggy-back sequence of thrust sheets

detached along Upper Triassic and upper Eocene evaporites (Figure 1c) (Sans, 2003; Séguret, 1972; Vergés et al., 1992).

Prior to the Alpine compression, the north Iberian margin was affected by lithosphere extension during the Late Triassic-Early Jurassic, favouring the development of extensive carbonate platforms (Aurell et al., 2002; Mey et al., 1968; Peybernès, 1976). During the Late Jurassic-Early Cretaceous, the reactivation of the Pyrenean rifting induced diapirism by the flow of Upper Triassic evaporites and the formation of salt-bearing basins (Canérot et al., 2005; Ferrer et al., 2012; Izquierdo-Llavall et al., 2020; Labaume & Teixell, 2020; Saura et al., 2016; Serrano & Martínez del Olmo, 1990; Vergés et al., 2019). In the North Pyrenean Zone, lithosphere hyperextension occurred, and upper mantle rocks were intruded below the sedimentary cover during the Late Aptian and beginning of the Late Cretaceous (Clerc & Lagabrielle, 2014; Clerc et al., 2016; Ford & Vergés, 2021; Lagabrielle et al., 2010). A recent study in the eastern North Pyrenean Zone demonstrated the significant role of diapirism during the Jurassic and Lower Cretaceous for the development of tectonic structures (Ford & Vergés, 2021). Late Jurassic-Early Cretaceous rifting was followed by asymmetric post-rift thermal contraction throughout the Pyrenees prior to the Alpine compression (Lescoutre et al., 2019; Martín-Chivelet, 2002).

The Upper Pedraforca thrust sheet consists of 1.6 km of Upper Triassic, Jurassic and Cretaceous rocks overthrusting Upper Cretaceous to Palaeocene syn-orogenic sediments (Vergés et al., 2002). These rocks are similar to those of its western equivalent, the Bóixols thrust sheet (García-Senz, 2002; Mencos et al., 2015) and are divided into pre-rift, syn-rift and post-rift marine sediments and marine to continental syn-orogenic sediments (Figure 2). The pre-rift sequence is composed of Triassic and Jurassic rocks. Triassic units consist of Keuper facies evaporites and clays, which acted as the main detachment level in the Pyrenees, and laminated dolostones from the Isàvena Formation (Arnal et al., 2002; Calvet et al., 1993; Séguret, 1972). The Bonansa Formation consists of Lower Jurassic dolomitic breccias, laminated limestones and dark marls with brachiopods and ammonoids, and Middle to Upper Jurassic dolostones (Aurell et al., 2002; Peybernès, 1976). The syn-rift sequence comprises Lower Cretaceous rocks and consists of Berriasian breccias and Valanginian to Albian limestones and marls (García-Senz, 2002). The post-rift sediments are the Cenomanian-Turonian Santa Fe Formation and lower Santonian limestones with *Lacazina* of the Sant Corneli Formation (Mey et al., 1968; Skelton et al., 2003; Ullastre & Masriera, 2004). The syn-orogenic sequence is made up by Upper Cretaceous to Palaeocene rocks. The Upper Cretaceous units consist of marine marls, limestones and carbonate breccias of the Upper Santonian to Maastrichtian Areny Formation, which is conformably



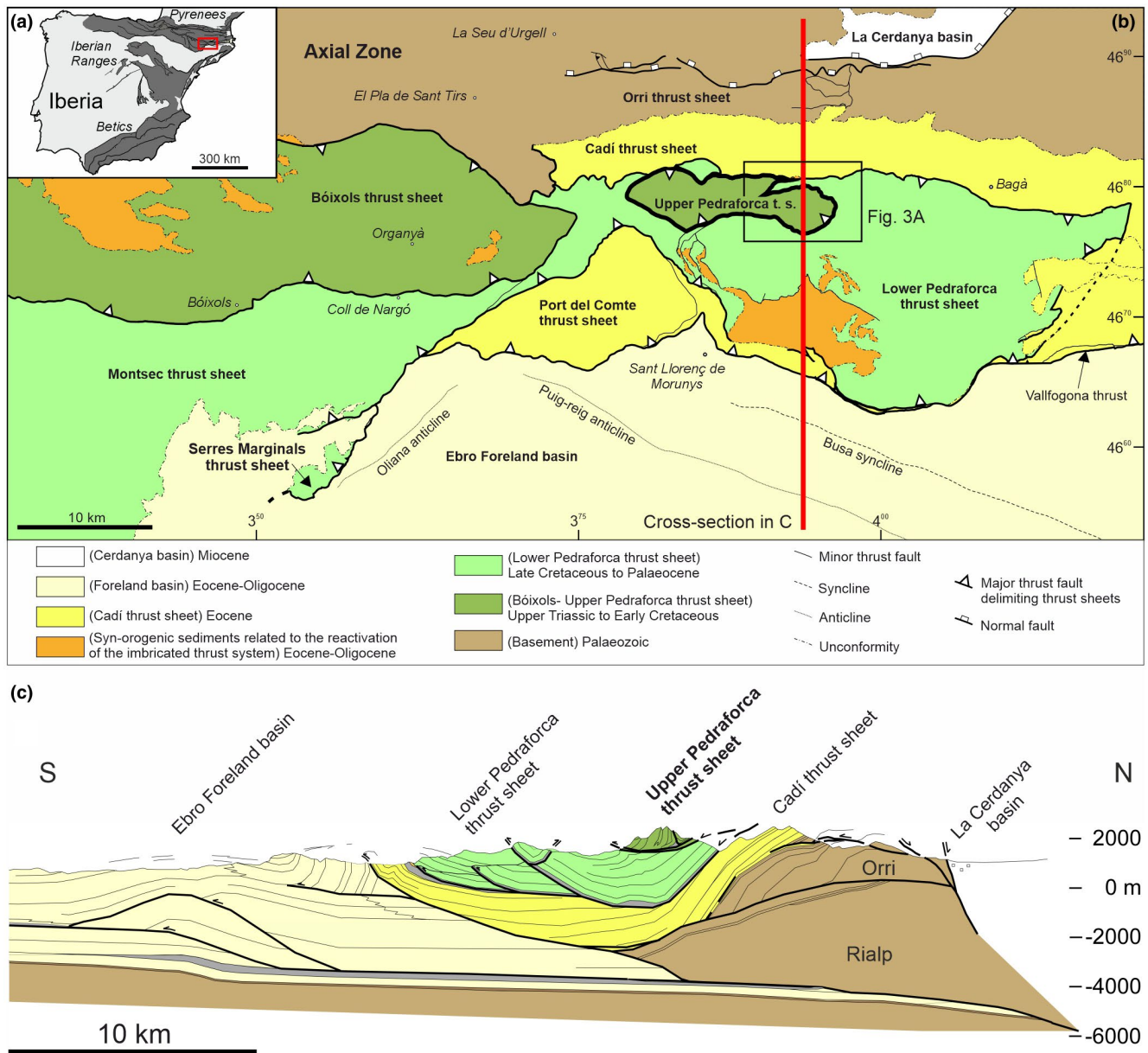


**FIGURE 1** (a) Regional map of the Iberian Peninsula showing the location of the south Pyrenean fold and thrust belt (red box). (b) Simplified geological map showing the main structural units forming the south Pyrenean fold and thrust belt. Based on Mató et al. (1994), Muñoz et al. (1994), Vergés et al. (1994) and Pi et al. (2001). The thick red line indicates the location of the composite cross-section in Figure 1c. The black box indicates the location of Figure 3a. (c) Geological cross-section of the Lower Pedraforca thrust sheet from Vergés (1993). Evaporite units are indicated in grey

overlain by the Maastrichtian to Danian marine dark marls, coastal siltstones and continental sandstones and conglomerates of Garumnian Facies (Puigdefàbregas & Souquet, 1986; Vicente et al., 2015).

### 3 | METHODOLOGY

Field work consisted of fracture and bedding orientation data acquisition and sampling of 87 fracture-filling

carbonate minerals and host rocks for petrographic observations and geochemical analyses. For structural analysis, fracture orientation measurements were plotted and restored with respect to bedding, when necessary, and their associated palaeostress field orientations were estimated using Win-Tensor software (v5.8.8.) (Delvaux & Sperner, 2003). Petrographic observations on 94 polished thin sections of fracture-filling carbonates and host rocks were carried out using optical and cathodoluminescence microscopy. A CL Technosyn cathodoluminescence



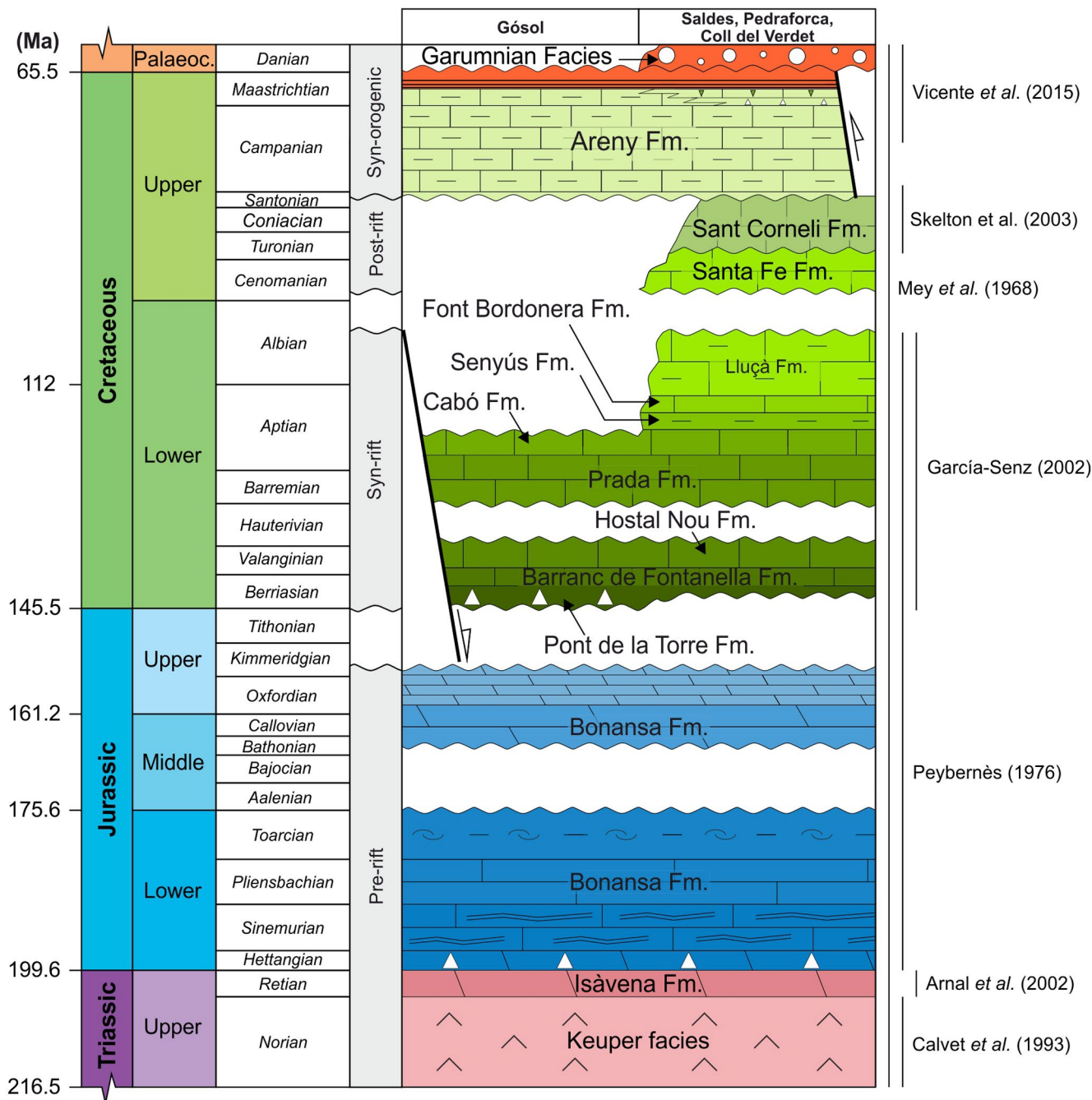


**FIGURE 2** Chronostratigraphic diagram showing the main sedimentary units of the Upper Pedraforca thrust sheet and their related tectonic events. The age of sedimentary units has been defined according to Mey *et al.* (1968), Peybernès (1976), Puigdefàbregas and Souquet (1986), Calvet *et al.* (1993), Arnal *et al.* (2002), García-Senz (2002), Skelton *et al.* (2003) and Vicente *et al.* (2015)

device Model 8200 MkII operating at 15–18 kV and 350  $\mu$ A gun current was used to distinguish different cement phases.

To decipher the geochemical signature of fluids that precipitated carbonate cements and that of their host rocks, carbon, oxygen, clumped and strontium isotopes and rare earth elements were analysed. These methods are summarized in Table 1, while the analytical procedure,

data treatment and standard errors are explained in detail in the supplementary material.

Four localities (Gósol, Pedraforca, Coll del Verdet and Saldes) were selected for this study due to the presence of deformation patterns related to both the Mesozoic extension and the Late Cretaceous-Oligocene compression events (Figure 3). Structural data acquisition and sampling were carried out at each locality. Field images of

TABLE 1 Summary of the geochemical methods used in this study to infer fluid signatures

Analytical method	Device	Number of samples	Type of results
Carbon and oxygen isotopes	Automated Kiel Carbonate Device attached to a Thermal Ionization Mass Spectrometer Thermo Electron (Finnigan) MAT-252	Replacive dolomite: 12	$\delta^{13}\text{C}$ and $\delta^{18}\text{O}$ composition of carbonate host rocks, calcite and dolomite cements
		Limestones: 20	
		Dolomite cement: 10	
		Calcite cement: 90	
Calcitized dolomite: 2			
Clumped isotope thermometry	Automated Thermo Scientific MAT 253 mass spectrometer (Thermo Fisher GmbH)	Dolomite cement: 2	Temperature of cement precipitation and $\delta^{18}\text{O}_{\text{fluid}}$
		Calcite cement: 7	
Strontium isotopes	TIMS-Phoenix mass spectrometer	Replacive dolomite: 3	$^{87}\text{Sr}/^{86}\text{Sr}$ ratios of carbonate host rocks, calcite and dolomite cements
		Limestones: 8	
		Dolomite cement: 3	
		Calcite cement: 12	
Elemental analysis	High-resolution inductively coupled plasma-mass spectrometry (HR-ICP-MS) Thermo Scientific, model Element XR	Replacive dolomite: 3	Rare Earths and Yttrium content (REE+Y) of carbonate host rocks, calcite and dolomite cements
		Limestones: 6	
		Dolomite cement: 2	
		Calcite cement: 9	

Note: The device used, the number of analyses and the type of results are included.

each locality are shown in Figure S1 of the supplementary material.

The Gósol locality lies north of the Gósol village. It consists of an ENE-WSW syncline formed by Jurassic carbonates within the Upper Pedraforca thrust sheet (Figure S1a). These Jurassic rocks are unconformably overlain by (1) Lower Cretaceous breccias and limestones and (2) Upper Cretaceous marls and limestones (Figures 3a and S1a,b). Upper Cretaceous sediments are overthrust by Jurassic carbonates at the south of the Gósol locality.

The Pedraforca locality lies 3 km to the northwest of Saldes village and corresponds to the damage zone of the Upper Pedraforca basal thrust, where Campanian carbonate breccias are affected by reverse and strike-slip faults (Figure S1c). At the Pedraforca locality, the Upper Pedraforca basal thrust is dipping to the south by the regional folding of the thrust sheet system above the basement-related stack of the Pyrenean Axial Zone (Figure 3b).

The Coll del Verdet locality corresponds to the internal part of the Upper Pedraforca thrust sheet (Figure 3a,b). Its structure consists of subvertical beds of Lower Jurassic limestones and marls and Middle to Upper Jurassic sucrose dolostones corresponding to a secondary weld zone (Saura et al., 2016). These rocks are unconformably overlain by carbonate breccias, partly replaced by dolomite, and a thick succession of Lower Cretaceous limestones (Figure S1d).

The Saldes locality, located between the villages of Gósol and Saldes (Figure 3), corresponds to the Upper Pedraforca thrust front and is in a structural position equivalent to the Pedraforca locality. It consists of a thrust fault zone acting as a thrust boundary between Upper Cretaceous breccias, limestones, siltstones and sandstones in its hangingwall and Upper Cretaceous dark marls in its footwall (Figure S1e).

## 4 | RESULTS: FRACTURE, PETROLOGICAL AND GEOCHEMICAL ANALYSIS

### 4.1 | Host rocks

The rocks hosting calcite and dolomite veins, range from Jurassic to Late Cretaceous in age. Their petrography and geochemistry have been studied, resulting in the identification of three types of replacive dolomite according to their age, based on previous stratigraphic studies (e.g. Peybernès, 1976) and their texture, based on petrographic observations. These dolostones are named in this study as Rd1 (Jurassic), Rd2 (Early Cretaceous) and Rd3 (Eocene), and are locally affected by calcitization (Ddol).

Jurassic rocks comprise limestones and dolostones of the Bonansa Formation, which was described by Peybernès (1976) and Aurell et al. (2002). This formation includes:

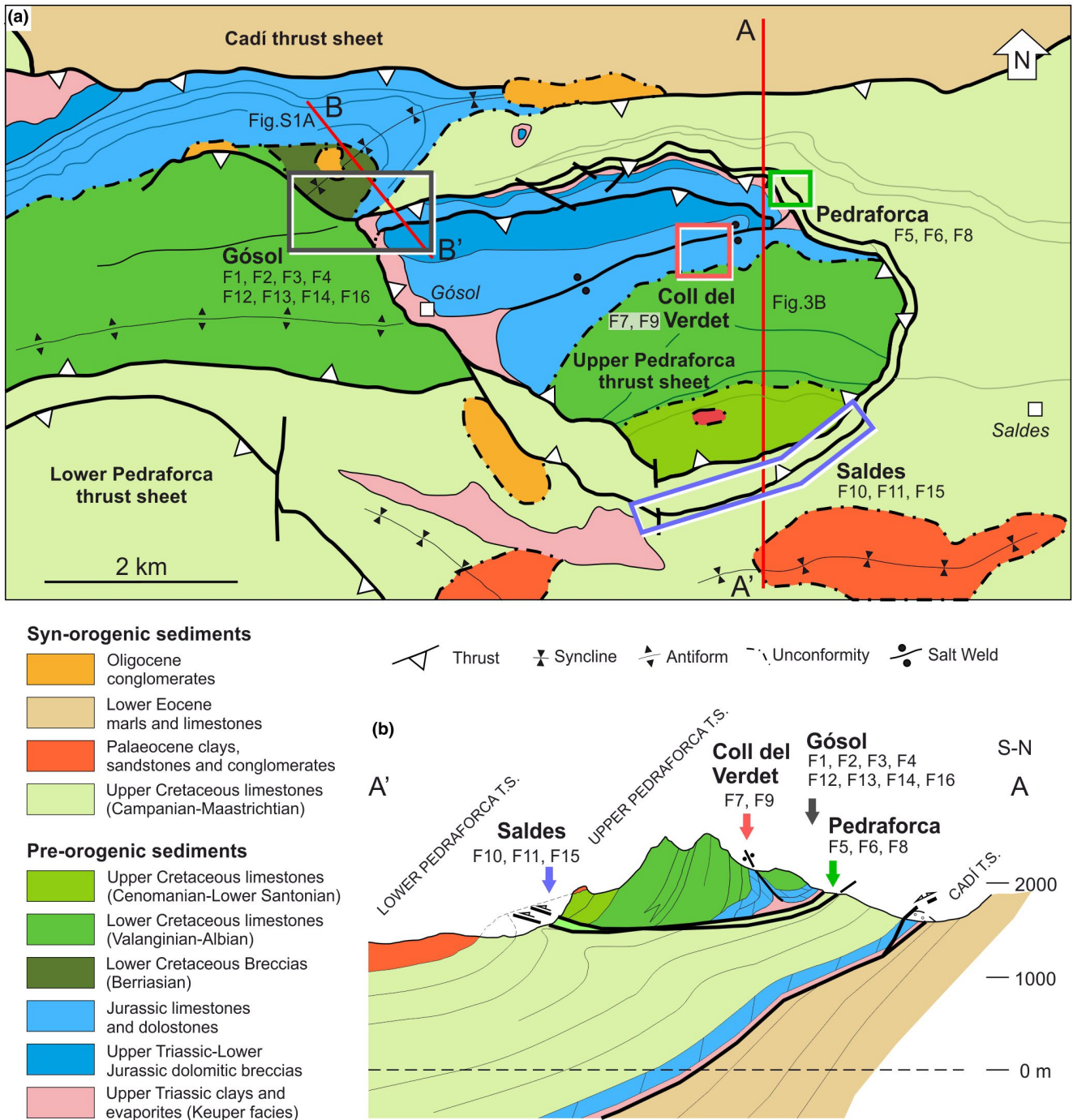


**FIGURE 3** (a) Structural sketch based on Martínez et al. (2001) of the studied area with the location of the studied localities (coloured boxes). Reference colours for each locality is the same than in Figures 5, 11–14. Cross-sections A–A' is shown in Figure 3b, whereas section B–B' is shown in Figure S1a. (b) Detailed geological cross-section of the Upper Pedraforca thrust sheet from Vergés (1993) showing the structural position of the studied localities (grey arrows). The location of the different fracture sets described in this study is indicated in each outcrop for both images

(1) Hettangian breccias replaced by dolomite Rd1, with crystals ranging between 15 and 30  $\mu\text{m}$  in size, and exhibiting idiotopic and hypidiotopic textures, (2) Sinemurian alternations of micritic mudstones and detrital carbonates with accessory quartz with mm-thick planar lamination and ripples (Figure 4a), (3) Toarcian dark marls and

peloidal grainstones with echinoid fragments partly replaced by up to 60  $\mu\text{m}$ -width euhedral dolomite crystals (Figure 4b), and (4) Middle and Upper Jurassic Rd1 dolostones. Middle Jurassic dolostones Rd1 are composed of subhedral crystals with sizes ranging from 200 to 400  $\mu\text{m}$  and exhibiting idiotopic and hypidiotopic textures (Figure 4c).



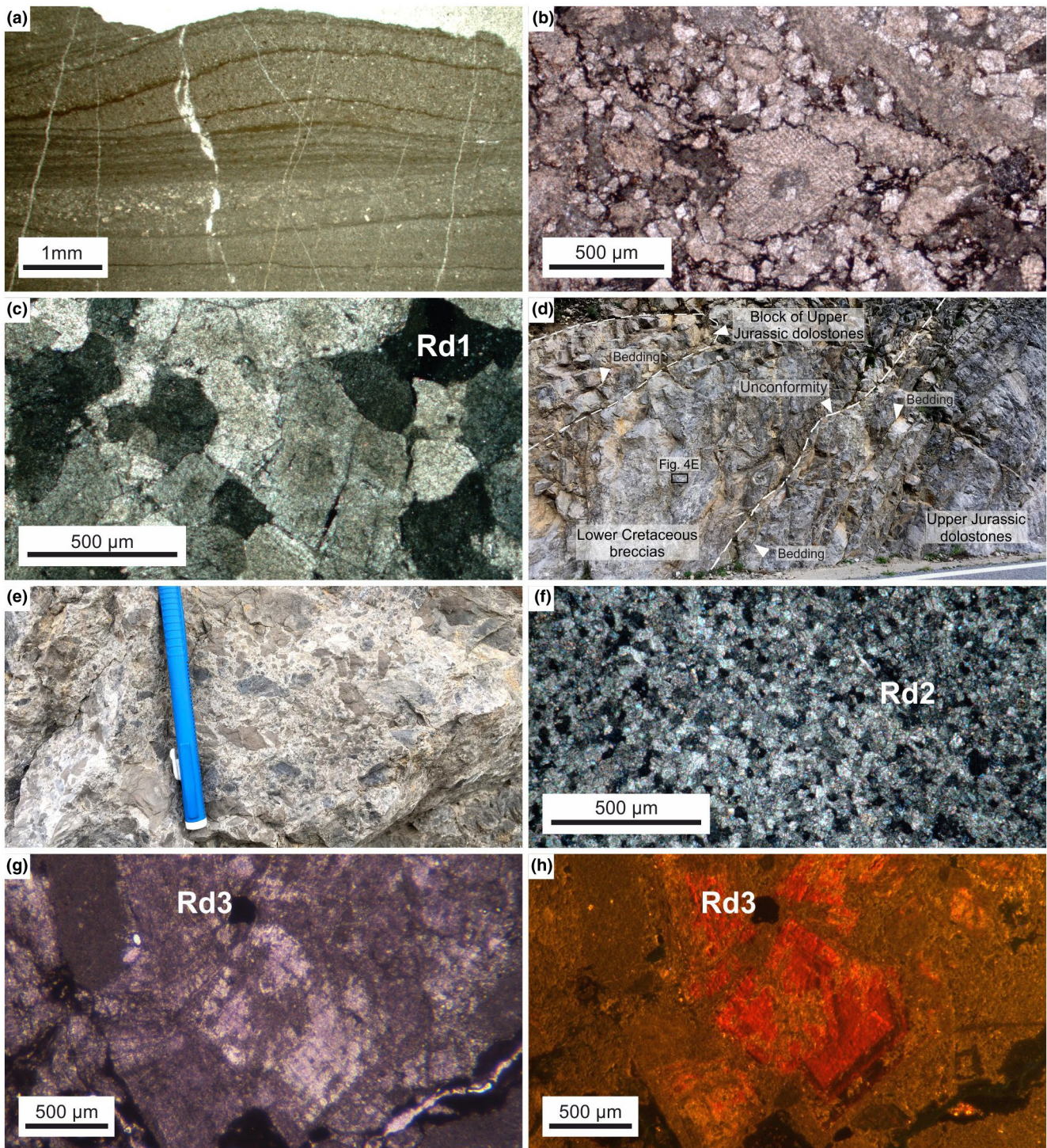


**FIGURE 4** Images from polarizing optical (PPL) and cathodoluminescence (CL) microscopy of the main textural features of the studied host rocks. (a) Sinemurian alternations of micritic mudstones and detrital carbonates with ripples and planar lamination. (b) Toarcian grainstone partially replaced by euhedral dolomite crystals. (c) Rd1 Middle Jurassic sucrose dolostones with idiotopic and hypidiotopic textures (crossed nicols). (d) Lower Cretaceous breccias unconformably overlain upper Jurassic dolostones. (e) Detail of (d). (f) Rd2 Upper Cretaceous dolostones exhibiting idiotopic and hypidiotopic textures (crossed nicols). (g, h) PPL and CL images of saddle dolomite Rd3 replacing carbonate breccias made of Sinemurian mudstones

Locally, dolomite Rd1 is completely calcitized (Ddol) and millimetre-size vugs filled with calcite are present. Upper Jurassic dolostones Rd1 are well-bedded and show

idiotopic and hypidiotopic textures, bivalve moldic porosity cemented by dolomite and centimetre-size vugs filled with calcite.



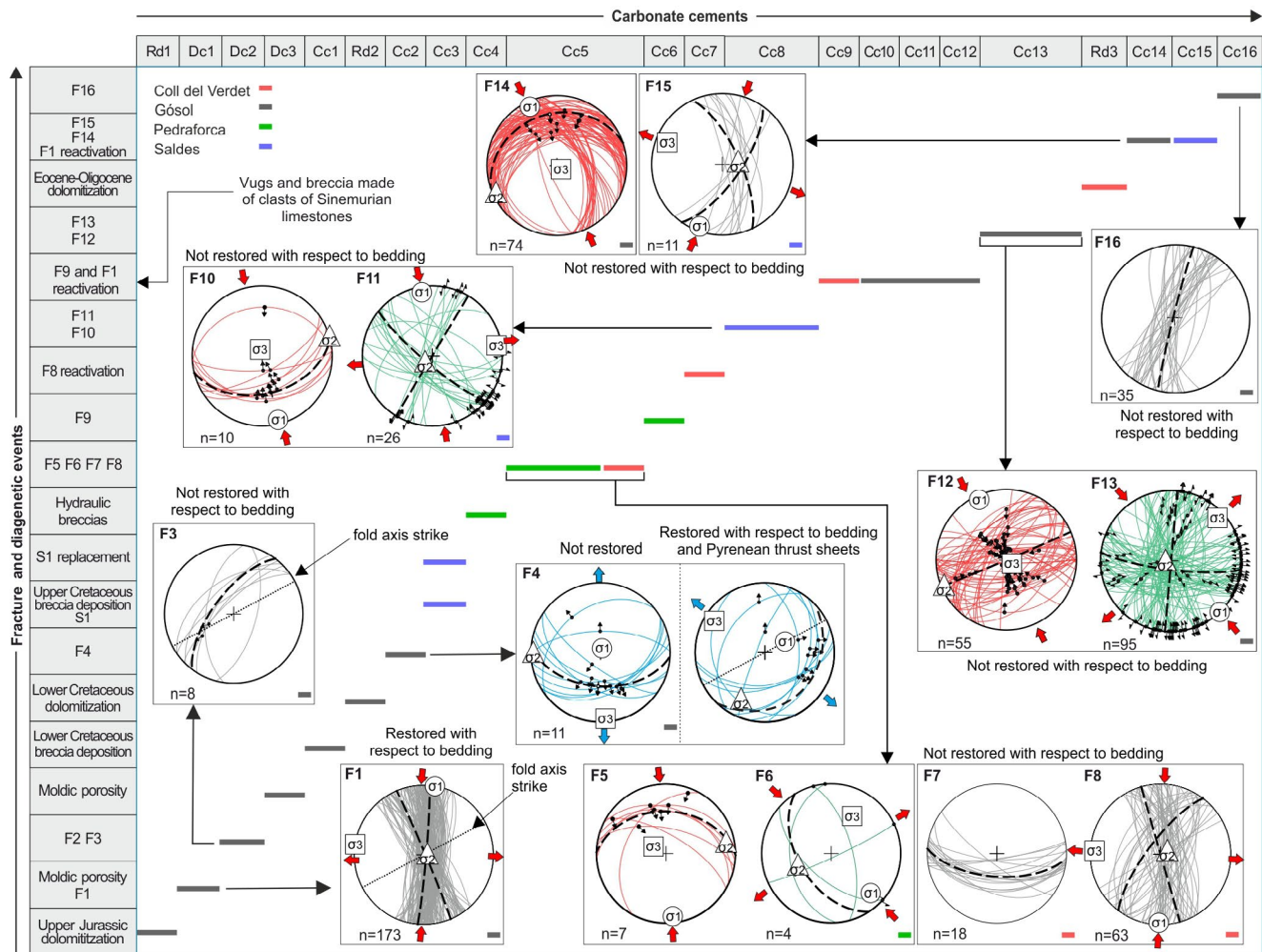


**FIGURE 5** Lower hemisphere Schmidt stereoplots of fracture-oriented data from the four localities with their associated diagenetic and tectonic stages. Zooms of the stereoplots and the estimated palaeostress field orientations for each fracture system are also displayed. The coloured lines represent each studied locality (dark grey is Gósol, green is Pedraforca, red is Coll del Verdet and blue is Saldes). Reference colours for each locality is the same than in Figures 3, 11–14. Red and blue arrows in the stereoplots represent the compressional stresses for reverse and strike-slip faults and for normal faults, respectively

The Lower Cretaceous rocks include (1) breccias of the Pont de la Torre Formation, unconformably overlying the Upper Jurassic dolostones Rd1 (Figure 4d), which are constituted by centimetre- to metre-scale fragments of Jurassic limestones and dolostones, sandy matrix made of dolomite, calcite and accessory quartz, as well as Lower Cretaceous wackestones with *Trocholina* (fragment sizes ranging from a few millimetres to metres; Figure 4e); and (2) well-bedded Rd2 dolostones with crystals ranging between 15 and 30  $\mu\text{m}$  in size and showing idiotopic and hypidiotopic textures (Figure 4f). At Coll del Verdet (Figure 3), the Lower Cretaceous breccias are partly replaced by Rd2.

Upper Cretaceous rocks are constituted by (1) carbonate breccias from the Areny Formation with fragments of mudstones and wackestones with rudists locally cemented by red micrite, which in this study is called sediment S1,

(2) dark marls with oysters and (3) yellow to reddish siltstones and sandstones with dinosaur egg fragments from the Garumnian. Finally, the Sinemurian mudstones are partially dolomitized by Rd3 at Coll del Verdet. This dolomitization is characterized by up to 2 mm-width saddle crystals (Figure 4g,h) affecting brecciated zones cemented by a calcite cement yielding U-Pb Priabonian ages between  $37.1 \pm 0.7$  and  $34.4 \pm 0.9$  Ma (karstic breccias in Cruset, Vergés, et al., 2020).

## 4.2 | Fracture analysis

U-Pb dating of fracture-filling calcite and dolomite cements was carried out by Cruset, Vergés, et al. (2020) on samples from the Upper Pedraforca thrust sheet. In this study, five types of fractures were dated; (1) conjugated vein systems,



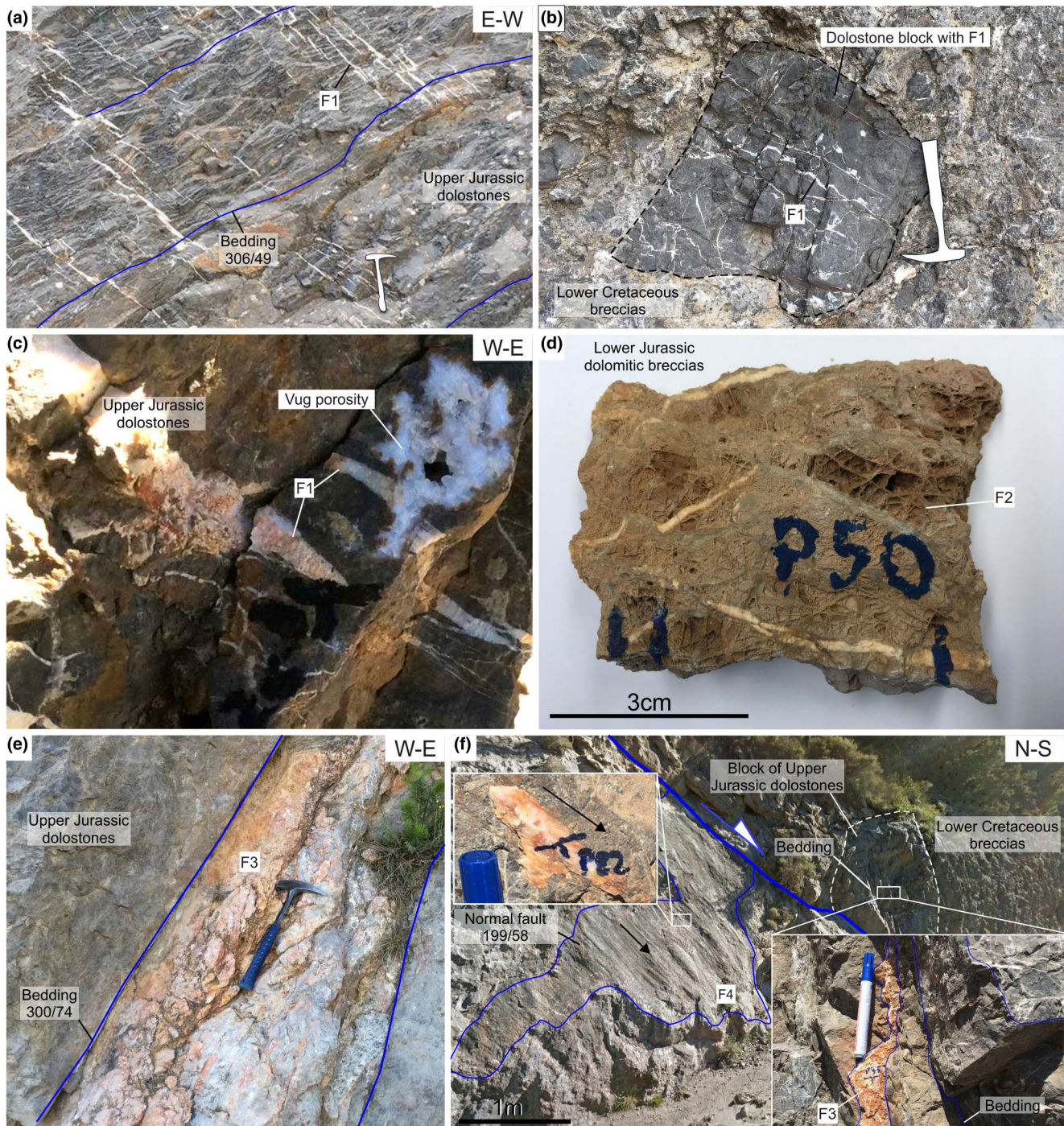


**FIGURE 6** Field images of F1, F2, F3 and F4 fracture sets at Gósol locality within the Upper Pedraforca thrust sheet. (a) F1 Bed-perpendicular N-S and NNW-SSE en-échelon vein arrays affecting Upper Jurassic dolostones. (b) Block of dolostones within Lower Cretaceous breccias containing F1 veins. (c) Vug porosities postdating F1 veins. (d) Dolostones from the basal part of Lower Jurassic affected by randomly oriented F2 fractures filled with dolomite and calcite cements. (e) F3 set sub-parallel to bedding of Rd1 dolostones. (f) E-W F4 normal faults affecting Lower Cretaceous breccias. Zoom images show F3 fractures included in Rd1 dolostones blocks and striae sets in normal faults

(2) veins parallel to bed strike, (3) normal faults, (4) reverse faults and (5) strike-slip faults. They yielded U-Pb dates between  $70.6 \pm 0.9$  Ma (Maastrichtian) and  $25.6 \pm 1.9$  Ma (Late Oligocene). The combination of these ages, together

with the well-established crosscutting relationships based on field and microstructural observations presented in this study (see below) allows the identification of 16 generations of fractures (F1 to F16; Figure 5). These 16 generations



include the five types of fractures described above, as well as randomly oriented veins.

The fracture sets F1, F2 and F3 are present at the Gósol locality and do not show clear crosscutting relationships with each other. Fracture set F1 consists of conjugate en-échelon vein arrays that display N-S and NNE-SSW strike after restoration with respect to bedding (Figures 5 and 6a), and are almost perpendicular to the axis of the syncline affecting Upper Jurassic dolostones (Figure 3a). They are bed-perpendicular regardless of bedding dip, show extensional openings of up to 2 cm and are cemented by dolomite, as well as by calcite when F1 are reactivated. The palaeostress field orientations indicate N-S strike-slip movement. F1 only affects Lower to Upper Jurassic rocks. This set of veins is also present in blocks of Rd1 dolostones within Lower Cretaceous breccias and cut by vug porosities filled with calcite (Figure 6b,c). Fracture set F2 are randomly oriented veins filled with dolomite and younger calcite cement, showing openings of a few millimetres to 2 cm (Figure 6d). These veins affect the lowermost part of the Jurassic dolomitic breccias. Fractures in the set F3 consist of bed-parallel veins and veins that crosscut bedding at a low angle (Figures 5 and 6e). They are cm-thick discrete fractures, which locally develop fault breccias cemented by dolomite. F3 fractures affect Jurassic rocks and are found concentrated within the SE limb of the syncline near the Gósol locality (Figures 3 and S1a,b). As F1 fracture set, the F3 fractures are also present in metre-scale blocks of Upper Jurassic dolostones within Lower Cretaceous sedimentary breccias in this area (Figure 6f).

The fractures of set F4 are E-W normal faults, that dip up to 50°, predominantly to the south, and consist of discrete slipping planes showing dip-slip striae sets and stepped slickensides (Figures 5 and 6f). Estimated palaeostress field orientations indicate N-S extension. However, the original orientation and dip of these fractures is not known. The restoration of the F4 fault set orientations with respect to bedding and the Pyrenean thrust sheets, which are tilted around 60° to the south, results in a mean dip of 25° and a NE-SW strike. Despite this restoration, kinematic indicators of F4 faults also indicate a normal sense of shear, suggesting that they were extensional in origin. (Figure 5). In this locality, F4 faults cut Lower Cretaceous breccias that postdate fracture sets F1 and F3 (Figure 6b,f).

Fracture set F5 consists of reverse faults formed within the damage zone of large thrusts within the Upper Pedraforca thrust sheet. They are WNW-ESE-trending isolated planes that dip to the north at a low angle and are filled with calcite (Figure 5). At some locations, reverse faults F5 develop foliated fault zones that indicate the sense of shear (Figure 7a). Palaeostress orientation estimation reveals N-S compression. F5 fractures are only present at

the Pedraforca locality crosscutting Upper Cretaceous hydraulic breccias associated with the damage zone of the Upper Pedraforca basal thrust (Figure 7a). These breccias are composed of centimetre-size limestone clasts, without significant rotation of fragments, which generate in situ fragmentation textures.

Fractures of set F6 consist of NNW-SSE and ENE-WSW-oriented subvertical strike-slip faults cemented by calcite, which also cut the hydraulic breccias of the Pedraforca locality (Figure 7a). F6 fractures show sub-horizontal striae sets and their estimated palaeostress field orientations indicate NW-SE compression (Figure 5).

E-W calcite veins, present in the internal part of the Upper Pedraforca thrust sheet, constitute the F7 fracture set (Figures 5 and 7b). These veins are parallel to the bed strike, have openings of up to 1 cm, and crosscut the bedding of Lower Jurassic to Lower Cretaceous rocks at a low angle. F7 have only been found at the Coll del Verdet locality and crosscutting relationships between sets F5 and F6 have not been observed.

F8 fracture set consists of highly dipping NE-SW and NW-SE-oriented conjugated calcite veins. They locally show strike-slip displacement in the internal part of the Upper Pedraforca thrust sheet and locally cut the F7 set (Figure 7b). F8 veins have lengths from a few centimetres to several meters and are, in some locations, surrounded by cataclastic breccias (Figure 7c). These breccias expand tens of centimetres from fracture planes and are composed of millimetre-size fragments of sucrose dolostones cemented by calcite, which suffered microcracking and rotation. Palaeostress field orientations estimated from F8 structures reveal N-S strike-slip movement. F8 veins have only been observed at Coll del Verdet locality.

Fractures of set F9 are randomly oriented calcite veins that crosscut hydraulic breccias at the basal thrust of the Upper Pedraforca thrust sheet. They have openings of up to 2 mm and have been only observed at the Pedraforca locality.

Fractures of set F10 consist of E-W reverse faults that grew within the fault zone of a major reverse fault in the footwall of the Upper Pedraforca thrust sheet. They are discrete planes dipping between 30° and 70° to the south and, at some locations, to the north (Figures 5 and 7d). Estimated palaeostress field orientations indicate N-S compression. F10 veins have been observed at Saldes locality.

Fracture set F11 is formed by NE-SW and NW-SE strike-slip faults in the footwall of the Upper Pedraforca thrust, within the damage zones of large reverse faults (Figure 5). These faults are subvertical discrete slipping planes with stepped slickensides (Figure 7e) and formed under N-S-directed compression (Figure 5). F11 faults affect Upper Cretaceous breccias and marls at Saldes locality. These





**FIGURE 7** Outcrop images showing the main features of fracture systems F5, F6, F7, F8, F10, F11, F12, F13, F14, F15 and F16. (a) Interpreted image of the damage zone of the main basal thrust of the Upper Pedraforca thrust sheet at the Pedraforca locality, where reverse faults F5 and strike-slip faults F6 cutting cemented hydraulic breccias and foliated fault zones (zoom) are shown. (b) F8 set cutting F7 vein set at Coll del Verdè. (c) N-S F8 fractures and associated cataclastic breccias affecting Middle Jurassic dolostones (Coll del Verdè locality). (d) F10 reverse fault emplacing Upper Cretaceous breccias of the Areny Formation over Upper Cretaceous dark marls of the Garumnian (Saldes locality). (e) F11 dextral strike-slip fault affecting Upper Cretaceous breccias (Saldes locality). The small image shows how these fractures are enlarged by dissolution. (f) Reverse faults F12 and strike-slip faults F13 cutting Lower Cretaceous breccias at Gósol locality. (g) F14 reverse faults and F16 N-S open fractures affecting Lower Cretaceous breccias (Gósol locality). The zoom shows the kinematic indicators of F14. (h) F15 veins within Upper Cretaceous conglomerates at Saldes locality



fractures are locally enlarged by dissolution where they affect carbonates (Figure 7e).

Fracture set F12 consists of NE-SW reverse faults formed in the hangingwall of the Upper Pedraforca thrust sheet, present at the Gósol locality. They are discrete planes dipping between 50° and 85°, with kinematic indicators that reveal NW-SE-directed compression (Figures 5 and 7f). Extensional veins developed perpendicular to fracture walls associated with F12.

F13 fractures are N-S and E-W-trending strike-slip faults formed in the hangingwall of the Upper Pedraforca thrust sheet (Figure 5). These fractures are subvertical discrete shear planes with stepped slickensides, with calcite cement and formed under NW-SE-oriented compression (Figure 7f). F13 structures affect Upper Jurassic dolostones and Lower Cretaceous breccias at the Gósol locality.

Fracture system F14 is characterized by E-W and NE-SW reverse faults that dip between 16° and 60° to the north and northwest, although locally also show a N-S orientation (Figures 5 and 7g). They consist of discrete planes that exhibit dip-slip striae sets, stepped slickensides and calcite-cemented cataclastic breccias (Figure 7g). The estimated palaeostress field orientation reveals NW-SE-directed compression (Figure 5). F14 structures have only been observed at the Gósol locality cutting F12 and F13.

F15 set is formed by NNW-SSE and NE-SW conjugated calcite veins that dip between 50° and 90° towards the ENE and ESE (Figure 7h). These veins locally form en-échelon arrays, are part of the damage zone of a major fault postdating the Upper Pedraforca frontal thrust at the Salde localities (Figure 3a), and developed as a consequence of an NNE-SSW-directed horizontal compression (Figure 5).

F16 set consists of NNE-SSW fractures that dip between 60° and 90°, with a constant orientation regardless of bed dips (Figure 5). These fractures appear cemented by calcite. F16 fractures affect Jurassic and Lower Cretaceous rocks and postdate F14 at the Gósol locality (Figure 7g).

### 4.3 | Cement petrology and vein microstructures

The integration of the U-Pb dates in Cruset, Vergés, et al. (2020), with the fracture analysis, petrographic observations and geochemical data obtained in this study from carbonate cements, allows the identification of three generations of dolomite cement (Dc1 to Dc3) and 16 generations of calcite cement (Cc1 to Cc16) (Figure 5). The type of fracture where the studied cements precipitated

and their host-rock, mineralogy, texture, luminescence and crosscutting relationships, are listed in Table 2.

Shear, syntaxial and stretching veins have been identified in the Upper Pedraforca thrust sheet, following the classification of Bons et al. (2012). Shear veins are present in reverse and strike-slip faults F5, F6, F10, F11, F12 and F13 (Figures 9g,h and 10c,d). In these veins, elongate sparite crystals grow parallel to vein walls and that, at some places, laterally evolve to blocky crystals. Syntaxial veins occur in all types of fractures within the Upper Pedraforca unit, where the growth and the precipitation of blocky and bladed crystals occur from vein edges to the centre or from one edge to the other (e.g. Cc11 in Figure 8a,b). The same growth is present in moldic and vuggy porosities containing Dc1 and Dc3, Cc8, Cc11, Cc12 and Cc13. Stretching veins are very scarce and are present in F9 sets containing Cc6 (Figure 9c,d), although the same microstructure occurs locally in extensional veins associated with F12 that contain Cc13 and at the tip of F1 en-échelon veins containing Dc1.

## 4.4 | Geochemistry

### 4.4.1 | Carbon and oxygen isotopes

The maximum, minimum and mean  $\delta^{13}\text{C}$  and  $\delta^{18}\text{O}$  compositions of 117 samples including carbonate host rocks, calcite and dolomite cements, and calcite sediment filling fractures, between interparticle porosity in breccias and vuggy porosity are summarized in Table 3. The complete  $\delta^{13}\text{C}$  and  $\delta^{18}\text{O}$  dataset is listed in Table S1A and plotted in Figure 11a. Due to its small size, Cc10 could not be sampled. The comparison between the  $\delta^{18}\text{O}$  values of carbonate cements and their host rocks is shown in Figure S2 of the supplementary material.

The results reveal a depletion of  $\delta^{13}\text{C}$  from +1.93 to -1.19‰ VPDB and  $\delta^{18}\text{O}$  from -2.54 to -12.2‰ VPDB from Dc1 to Cc2 (Figure 11a). The same decreasing trend occurs from Cc3 to Cc6 (from +1.9 to -2.4‰ VPDB for  $\delta^{13}\text{C}$  and from -2.3 to -14.4‰ VPDB for  $\delta^{18}\text{O}$ ). Cc8 to Cc9 only show a decrease in  $\delta^{18}\text{O}$  (from -5.2 to -11.7‰). S1, Cc3 and Cc4, Cc8, Cc12 and Cc16 show  $\delta^{18}\text{O}$  values similar to that of their host rocks, whereas Cc5 and Cc6, Cc7, Cc9, Cc11, Cc13 and Cc14 have more depleted values (Figure S2).

### 4.4.2 | Clumped isotope thermometry

Dolomite cements Dc1 and Dc2 and calcite cements Cc4, Cc5, Cc8, Cc9, Cc11, Cc13 and Cc15 were analysed for clumped isotope thermometry (Tables 4, S2 and



TABLE 2 Main petrographic features of the carbonate cements within the Upper Pedraforca thrust sheet

Cement	Locality	Host-rock	Type of fracture	Mineralogy	Cement texture	Luminescence	U-Pb ages (Cruset, Vergés, et al., 2020)	Images and crosscutting relationships
Dc1	Gósol	Rd1 dolostones	F1 and moldic porosity	Dolomite	250 to 700 $\mu\text{m}$ saddle crystals	Red (Figure 8a,b)	–	Cut by Cc10 and Cc11 (Figure 8a,b)
Dc2	Gósol	Rd1 dolostones	F2 and F3	Dolomite	200 $\mu\text{m}$ to 2 mm saddle crystals	Non-luminescent to red	–	Cut by Cc11 (Figure 8c,d)
Dc3	Gósol	Rd1 dolostones	Moldic porosity	Dolomite	200 $\mu\text{m}$ to 1 mm saddle crystals	Red	–	No crosscutting relationships (Figure 8e,f)
Cc1	Gósol	Lower Cretaceous breccias	Interparticle porosity	Calcite	Up to 2 mm blocky crystals	Non-luminescent	–	Cementing Lower Cretaceous breccias (Figure 8g,h)
Cc2	Gósol	Lower Cretaceous breccias	F4	Calcite	200 to 500 $\mu\text{m}$ long elongated crystals parallel to fracture walls	Non-luminescent to dull brown (Figure 8i,j)	–	Cut Lower Cretaceous breccias with Dc1 to Dc3 fragments
Cc3	Saldes	Upper Cretaceous carbonate breccias	Interparticle porosity	Calcite	Microsparite	Non-luminescent	–	Replacing S1 (Figure 9a,b)
Cc4	Pedraforca	Upper Cretaceous limestones	hydraulic breccias in main thrust fault zone	Calcite	400 $\mu\text{m}$ to 1 mm blocky crystals	Non-luminescent to orange	70.6 $\pm$ 0.9 Ma	Cut by Cc6 (Figure 9c,d)
Cc5	Pedraforca and Coll del Verdets	Upper Cretaceous limestones	F5 and F6 (Pedraforca) F7 and F8 (Coll del Verdets)	Calcite	Up to 3 mm long elongated crystals parallel to fracture walls	Non-luminescent to dull orange	68.2 $\pm$ 2.0 to 55.3 $\pm$ 0.5 Ma	Cut hydraulic breccias with Cc4 (Figure 7a,b) and cut by Cc7 and Cc9 (Figure 9e,f and i,j)
Cc6	Pedraforca	Upper Cretaceous limestones	F9	Calcite	20 to 100 $\mu\text{m}$ blocky crystals	Non-luminescent	–	Cut Cc4 (Figure 9b,c)
Cc7	Coll del Verdets	Rd1 dolostones	F8	Calcite	300 $\mu\text{m}$ to 3 mm blocky crystals	Non-luminescent to orange	47 $\pm$ 10.5 to 38.8 $\pm$ 1.1 Ma	Cut Cc5 (Figure 9e,f)
Cc8	Saldes	Upper Cretaceous carbonate breccias	F10, F11 and vuggy porosity	Calcite	Up to 1 mm long elongated sparite parallel to fracture walls and 2 mm long bladed crystals (Figure 9g,h)	Dull-orange	38.2 $\pm$ 1.4 Ma	Evolves gradually to Cc9 in F11 enlarged fractures

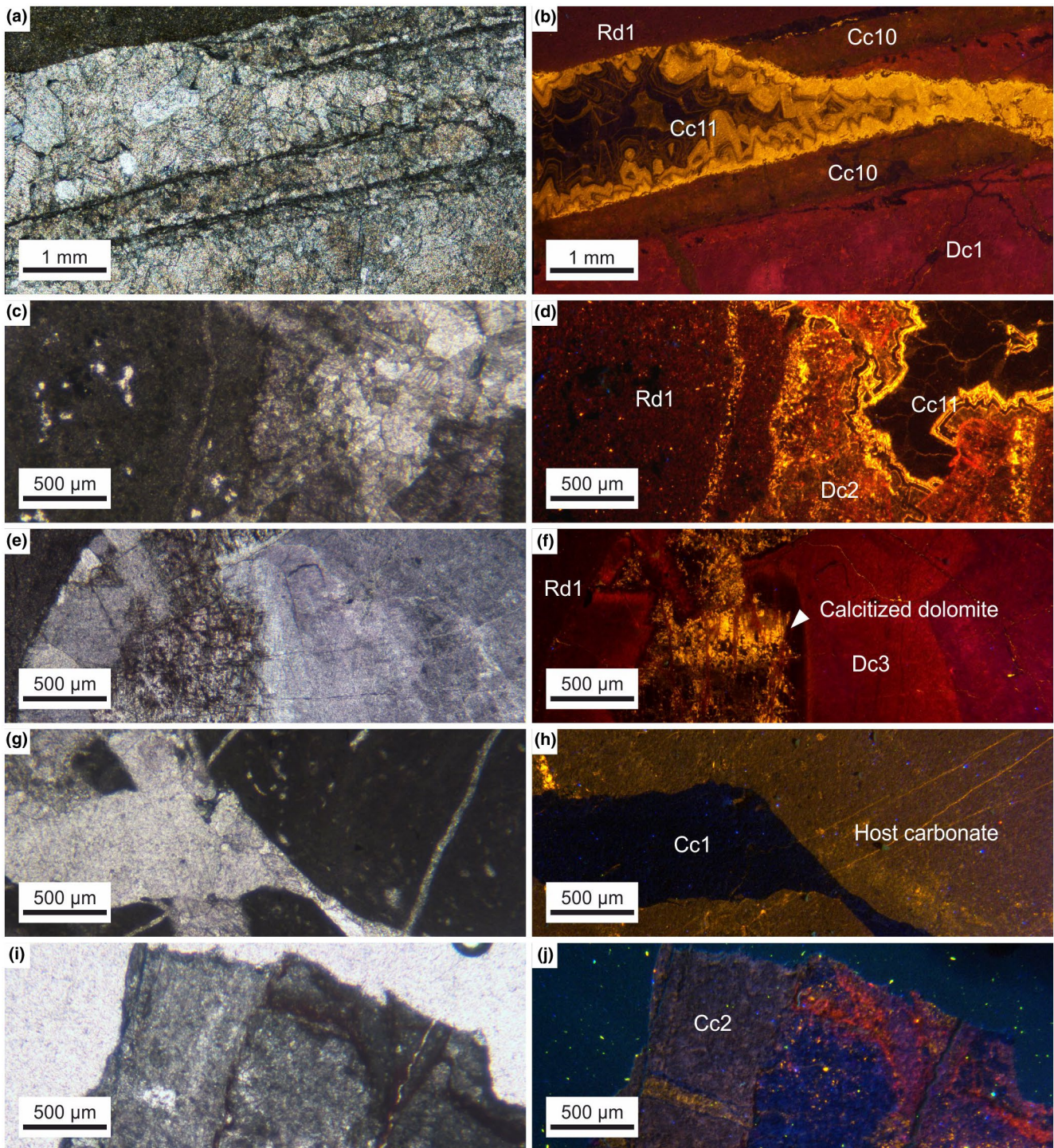
(Continues)

TABLE 2 (Continued)

Cement	Locality	Host-rock	Type of fracture	Mineralogy	Cement texture	Luminescence	U-Pb ages (Cruset, Vergés, et al., 2020)	Images and crosscutting relationships
Cc9	Saldes and Coll del Verdè	Upper Cretaceous carbonate breccias and Lower Jurassic limestones	Reactivated F8	Calcite	Up to 2 mm long bladed crystals	Dull-orange to orange luminescent	35.8 ± 3 to 25.7 ± 2 Ma	Cut Cc5 (Figure 9i,j)
Cc10	Gósol	Rd1 dolostones	Reactivated F1	Calcite	100 µm blocky crystals	Dull-orange	35.1 ± 1.8 Ma	Cut Dc1 (Figure 8a,b)
Cc11	Gósol and Coll del Verdè	Lower Jurassic limestones, Rd1 dolostones and Lower Cretaceous breccia	Reactivated F1 and vuggy porosity (Gósol) Between breccia clasts (Coll del Verdè)	Calcite	150 to 800 µm blocky crystals	Non-luminescent to yellow or zoned dull-orange	37.11 ± 0.7 to 34.4 ± 0.9 Ma	Cut Dc1, Dc2 and Cc10 (Figure 8a–d)
Cc12	Gósol	Rd1 dolostones	Vuggy porosity	Calcite	Up to 500 µm blocky crystals	Zoned, dull-brown to non-luminescent	–	Cut Cc11 (Figure 10a,b)
Cc13	Gósol	Rd1 dolostones and Lower Cretaceous breccias	F12, F13 and vuggy porosity	Calcite	Up to 2 mm long elongated sparite parallel to fracture walls and blocky crystals	Dull-orange to orange luminescent	31.1 ± 1.4 Ma	Cut Cc11 and 12 (Figure 10a–d)
Cc14	Gósol	Lower Cretaceous breccias and Rd1 dolostones	F14 and reactivated F1	Calcite	100 µm to 1 mm blocky crystals	Dull-orange	–	Cut Cc11 (Figure 10e,f)
Cc15	Saldes	Garumnian red-sandstones	F15	Calcite	200 µm to 4 mm blocky crystals	Dull-orange	34.96 ± 16.5 Ma	No crosscutting relationships (Figure 10g,h)
Cc16	Gósol	Lower Cretaceous breccias	F16	Calcite	mm-sized blocky crystals	Non-luminescent	–	Cut Cc11 (Figure 10i,j) and F16 with Cc16 cut F14 with Cc14 (Figure 7g)

Note: The locality and type of fractures where they precipitated as well as their host-rock, mineralogy, texture, luminescence and crosscutting relationships are indicated. U-Pb dates from Cruset, Vergés, et al. (2020) measured in the Upper Pedraforca thrust sheet are also displayed.





**FIGURE 8** Images from polarizing optical (PPL) and cathodoluminescence microscopy (CL) of calcite and dolomite cements. (a, b) Cement Dc1 crosscut by Cc10 and Cc11 in F1 set. (c, d) Cement Dc2 cut by Cc11 in F2 vein sets. (e, f) Cement Dc3 locally calcitized and filling bivalve moldic porosity. (g, h) Cement Cc1 cementing Lower Cretaceous breccias. (i, j) Cement Cc2 precipitated in F4 normal faults

Figure 11b). The measured temperature and  $\delta^{18}\text{O}_{\text{fluid}}$  of cement Dc1 are  $149.4 \pm 12.5^\circ\text{C}$  and  $+11.2 \pm 1.1\%$  VSMOW, respectively. For Dc2, a lower temperature of  $79.7 \pm 12^\circ\text{C}$  is measured, whereas the  $\delta^{18}\text{O}_{\text{fluid}}$  of  $+7.1 \pm 0.7\%$  VSMOW are obtained. For Cc4, the measured

temperature is  $81 \pm 21.7^\circ\text{C}$ , whereas its  $\delta^{18}\text{O}_{\text{fluid}}$  is  $+6.6 \pm 3\%$  VSMOW. For Cc5, a similar temperature of  $79.7 \pm 12^\circ\text{C}$  is measured, whereas the  $\delta^{18}\text{O}_{\text{fluid}}$  of  $+3.1 \pm 1.7\%$  VSMOW is lower than that of Cc4. For calcite cement Cc8, the calculated temperature and



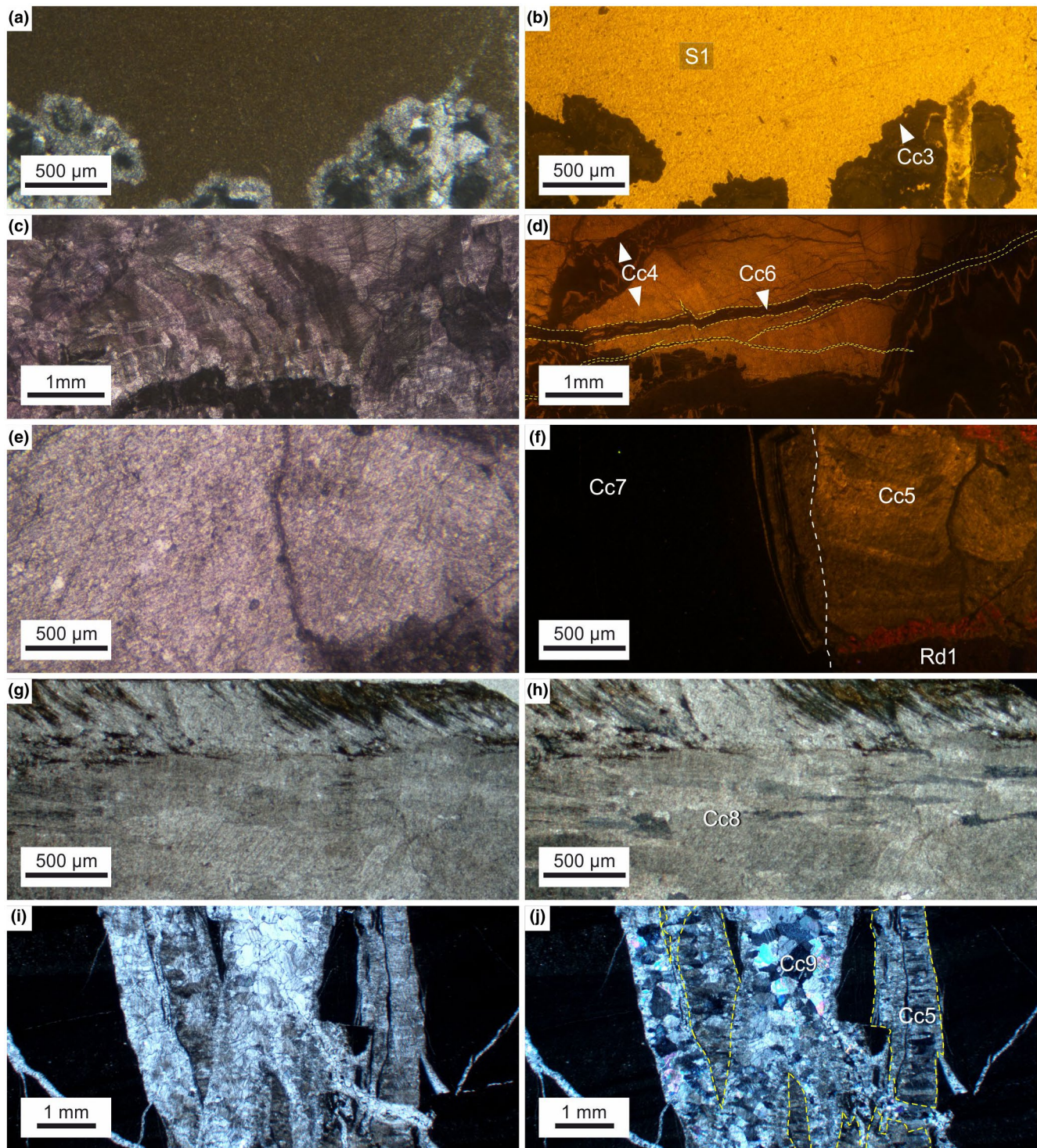


**FIGURE 9** Images from polarizing optical (PPL) and cathodoluminescence microscopy (CL) of calcite cements. (a, b) Cement Cc3 replacing S1 red micrite within the intergranular porosity of the Upper Cretaceous breccias. (c, d) Cement Cc4 cement in hydraulic breccias within the main thrust fault of the Upper Pedraforca thrust sheet cut by Cc6 precipitated in the F9 set. (e, f) Cc5 cement in F7 veins cut by Cc7 precipitated in F8 veins. (g, h) Elongated sparite parallel to fracture walls of F11 strike-slip faults. (i, j) Reactivated F8 vein showing the crosscutting relationships between Cc5 and Cc9

$\delta^{18}\text{O}_{\text{fluid}}$  are  $100.78 \pm 4.2^\circ\text{C}$  and  $+9.4 \pm 0.6\text{‰}$  VSMOW, respectively. For Cc9, the calculated temperature is similar than that of Cc8 ( $101.4 \pm 5.0^\circ\text{C}$ ), whereas its  $\delta^{18}\text{O}_{\text{fluid}}$  is more depleted ( $+3.9 \pm 0.7\text{‰}$  VSMOW).

For Cc11, the calculated temperatures and  $\delta^{18}\text{O}_{\text{fluid}}$  range between  $23.3 \pm 2.3^\circ\text{C}$  and  $30.3 \pm 13.6^\circ\text{C}$  and between  $-3.6 \pm 2.7\text{‰}$  and  $-4.84 \pm 0.6\text{‰}$  VSMOW, respectively. For Cc13, the measured temperature and



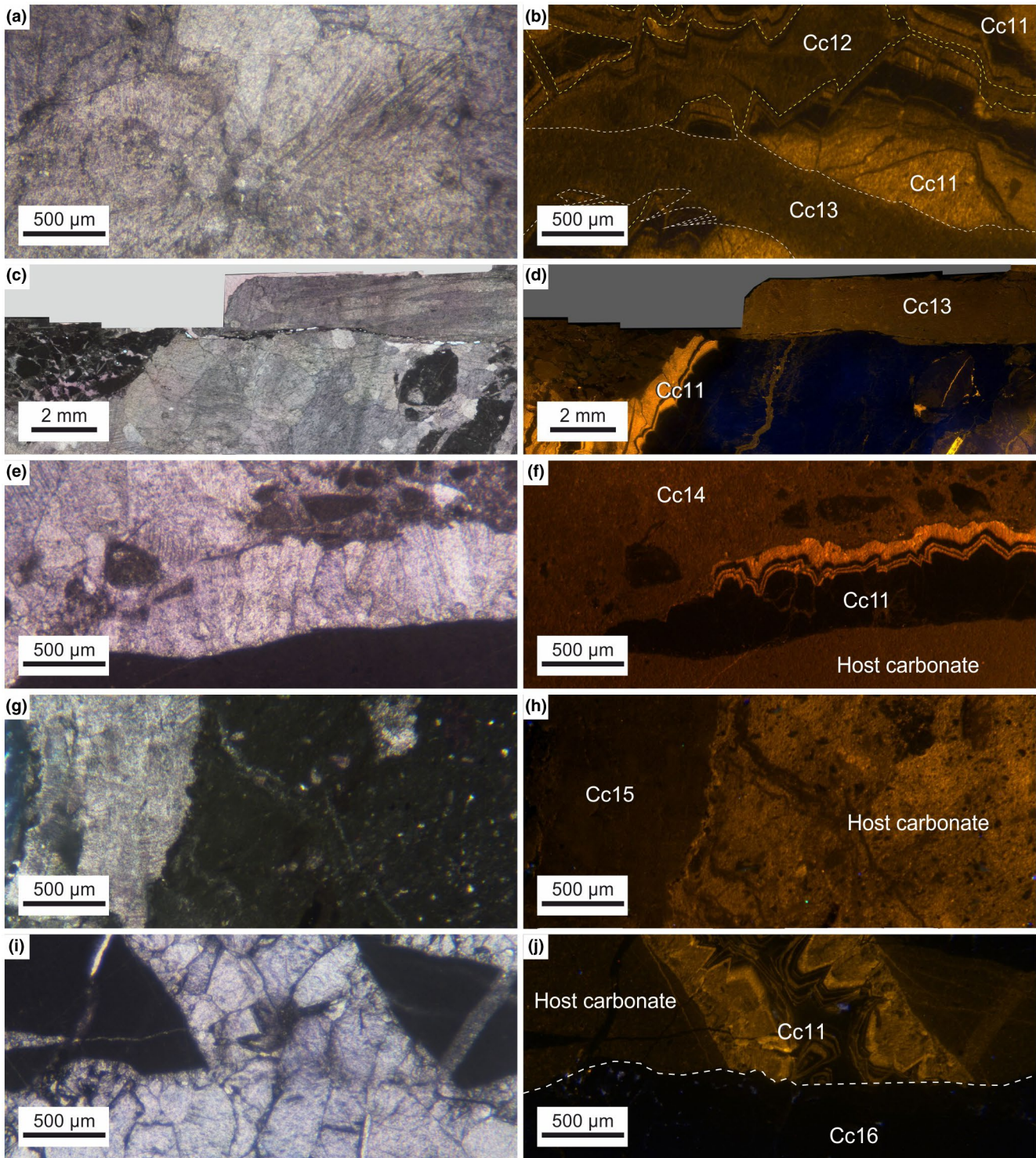


**FIGURE 10** Images from polarizing optical (PPL) and cathodoluminescence microscopy (CL) of calcite cements. (a, b) Vug porosity filled with Cc12 postdating Cc11. These cements are cut by cement Cc13 in a vein associated with F12 reverse faults. (c, d) Cement Cc13 in F12 reverse fault cutting Cc11 in vug porosity. (e, f) Cement Cc11 cut by Cc14 precipitated in F14 reverse faults. (g, h) Cement Cc15 precipitated in F15 veins. (i, j) Cement Cc16 in set F16 cutting cement Cc11

$\delta^{18}\text{O}_{\text{fluid}}$  are  $52.2 \pm 7.1^\circ\text{C}$  and  $-3.6 \pm 1.2\text{‰}$  VSMOW, respectively. Cc15 has a measured temperature and  $\delta^{18}\text{O}_{\text{fluid}}$  of  $67.27 \pm 4.8^\circ\text{C}$  and  $-0.33 \pm 0.8\text{‰}$  VSMOW, respectively.

#### 4.4.3 | Strontium isotopes

The  $^{87}\text{Sr}/^{86}\text{Sr}$  ratios of Jurassic and Cretaceous limestones, replacive dolostones Rd1 and Rd2, sediment S1, dolomite

TABLE 3 Minimum, maximum and mean  $\delta^{13}\text{C}$  and  $\delta^{18}\text{O}$  values of the carbonate host rocks, dolomite and calcite cements and calcite sediment in the Upper Pedraforca thrust sheet

Description	<i>n</i>	$\delta^{13}\text{C}$ ‰ VPDB <sub>min</sub>	$\delta^{13}\text{C}$ ‰ VPDB <sub>max</sub>	$\delta^{13}\text{C}$ ‰ VPDB <sub>mean</sub>	$\delta^{18}\text{O}$ ‰ VPDB <sub>min</sub>	$\delta^{18}\text{O}$ ‰ VPDB <sub>max</sub>	$\delta^{18}\text{O}$ ‰ VPDB <sub>mean</sub>
Lower Jurassic limestones	4	-0.2	0.8	0.22	-6.2	-4.4	-5.2
Rd1	9	-1.7	3	1.64	-3.3	0.6	-1.33
Rd2	2	0.1	1.7	0.91	-1.8	-1.7	-1.73
Upper Jurassic limestones	2	1.1	1.8	1.45	-3.6	-2.4	-2.97
Lower Cretaceous limestones	2	-1.7	1.4	-0.13	-3.6	-3.1	-3.37
Undifferentiated Cretaceous limestones	4	2.2	2.8	2.42	-6.1	-4.3	-5.04
Upper Cretaceous limestones	5	-2.2	1	-0.56	-8.6	-5.2	-6.62
Garumnian grey marls	1	-0.2	-	-	-5.6	-	-
S1	2	1.5	1.6	1.57	-4.9	-4.2	-4.51
Rd3	1	-0.3	-	-	-6.9	-	-
Ddol	2	-2.3	-0.9	-1.65	-7.4	-4.3	-5.83
Dc1	4	1.1	1.9	1.66	-4.8	-2.5	-3.96
Dc2	4	0.1	1.2	0.59	-6.9	-6.3	-6.65
Dc3	2	1.5	1.8	1.63	-8.9	-8.6	-8.77
Cc1	3	-1.2	-0.2	-0.78	-10.6	-8.1	-9.26
Cc2	3	-1	-0.6	-0.78	-12.2	-9.1	-11.25
Cc3	1	1.9	-	-	-2.3	-	-
Cc4	2	-2.4	1.3	-1.85	-5.95	-5.85	-5.9
Cc5	9	-0.9	0.4	-0.43	-14.4	-8.5	-11.19
Cc6	1	-1.4	-	-1.48	-6.1	-	-8.84
Cc7	9	-5.9	-1.1	-2.84	-9.1	-5.5	-7.44
Cc8	6	-0.8	1.7	0.51	-7.5	-5.2	-6.49
Cc9	7	-1.1	1.9	0.51	-11.7	-8.2	-9.1
Cc11	14	-3.5	-0.1	-1.5	-7.7	-3.8	-6.6
Cc12	1	-1.3	-	-	-0.8	-	-
Cc13	4	-0.7	0.9	0.1	-14.3	-9.6	-11.1
Cc14	3	-0.6	0.7	0	-6.6	-5.5	-5.97
Cc15	3	-6.2	-0.9	-4.29	-11.5	-9.2	-10.26
Cc16	7	-9.3	-2.2	-5.55	-8.2	-5.4	-6.81

Note: *n* represents the number of samples for each type of host rock, cement or sediment.

cements Dc1 and Dc2 and calcite cements Cc2, Cc3, Cc4, Cc5, Cc8, Cc9, Cc11, Cc13, Cc14 and Cc15 are presented in Tables 5 and S2 and in Figure 12.

Lower and Upper Jurassic limestones have  $^{87}\text{Sr}/^{86}\text{Sr}$  ratios of 0.708301 and 0.707343, respectively. Replacive dolomite Rd1 has an  $^{87}\text{Sr}/^{86}\text{Sr}$  ratio of 0.707816, whereas for Rd2 ranges between 0.707366 and 0.707604. For Upper Cretaceous limestones and sediment S1, this ratio ranges between 0.707526 and 0.708084 and between 0.707747 and 0.707951, respectively.

The  $^{87}\text{Sr}/^{86}\text{Sr}$  ratio for Dc1 is 0.707425, whereas Dc2 has higher ratios ranging between 0.708262 and 0.708354. Cc2 and Cc3 have ratios of 0.707857 and

0.707720, respectively. The  $^{87}\text{Sr}/^{86}\text{Sr}$  ratio of Cc4 ranges between 0.707563 and 0.707778, whereas a similar ratio of 0.707707 is obtained for Cc5. Slightly higher  $^{87}\text{Sr}/^{86}\text{Sr}$  ratios have been measured in Cc8 (0.707829), Cc11 (between 0.707829 and 0.707919), Cc14 (0.707933) and Cc15 (0.707751). The highest ratios have been obtained for Cc9 (0.709747) and Cc13 (0.708855).

#### 4.4.4 | REE and Y composition

The REE and Y contents for Jurassic dolostones, Upper Cretaceous limestones, sediment S1, dolomite cements



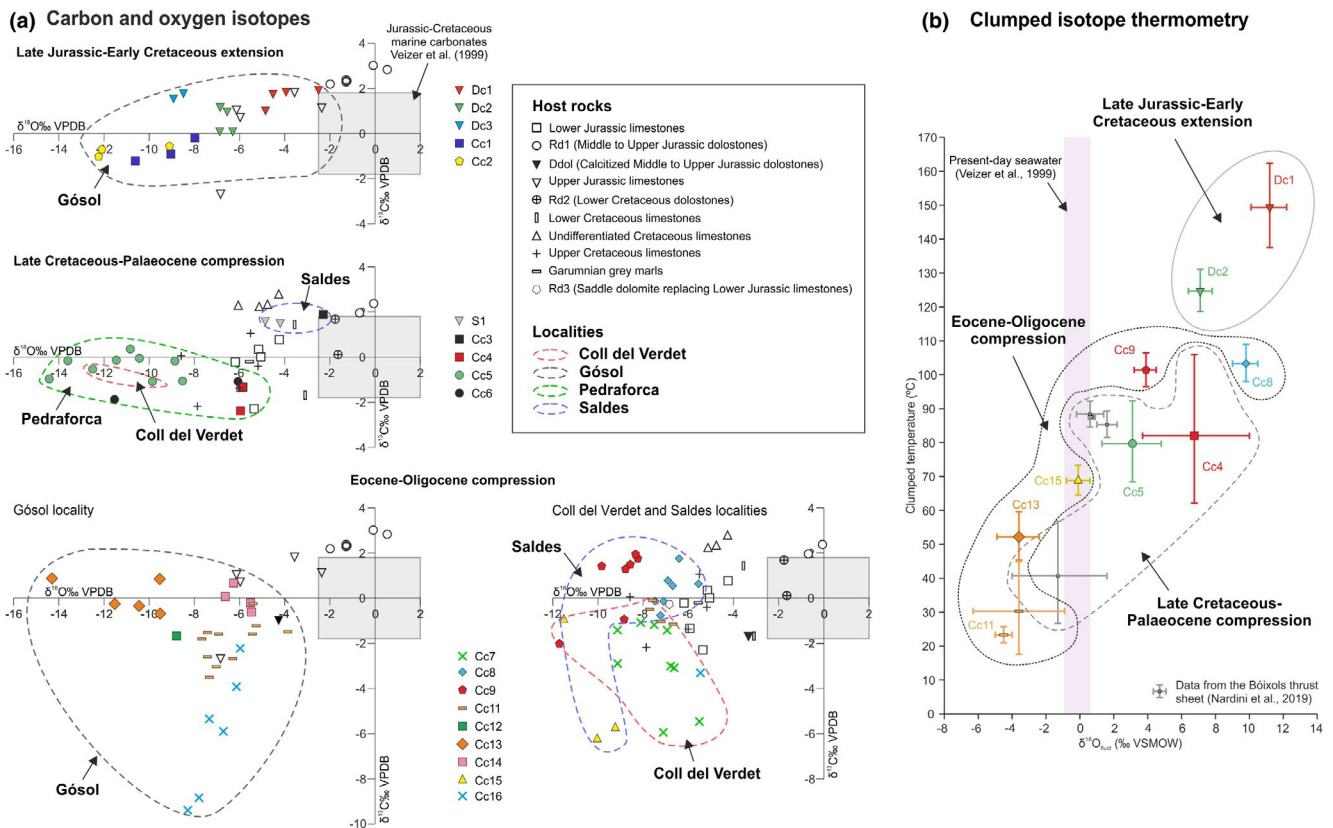


**FIGURE 11** (a)  $\delta^{18}\text{O}$  and  $\delta^{13}\text{C}$  cross-plots of carbonate host rocks, dolomite and calcite cements and calcite sediment from the Upper Pedraforca thrust sheet. The dashed coloured areas represent each locality. Symbols for each cement are the same than in Figures 12–14. Reference colours for each locality are the same than in Figures 3, 5, 12–14. (b) Clumped isotope temperatures ( $^{\circ}\text{C}$ ) versus calculated  $\delta^{18}\text{O}_{\text{fluid}}$  (‰ VSMOW) for the Upper Pedraforca thrust sheet. Clumped isotope data from Nardini et al. (2019) from the Bóixols thrust sheet is also shown for comparison.  $\delta^{18}\text{O}$  in present-day seawater in ‰ VSMOW is from Veizer et al. (1999)

**TABLE 4**  $\delta^{13}\text{C}$ ,  $\delta^{18}\text{O}$ ,  $\Delta_{47}$  and  $\delta^{18}\text{O}_{\text{fluid}}$  values of the dolomite cements Dc1 and Dc2, and calcite cements Cc4, Cc5, Cc8, Cc9, Cc11, Cc13 and Cc15 within the Upper Pedraforca thrust sheet

Sample	Outcrop	Type of cement	n	$\delta^{13}\text{C}$ ‰ VPDB	$\delta^{18}\text{O}$ ‰ VPDB	$\Delta_{47}$	T $^{\circ}\text{C}$	$\delta^{18}\text{O}_{\text{fluid}}$ ‰ VSMOW
P24	GS	Dc1	4	+1.8	−5.1	$0.458 \pm 0.014$	$149.4 \pm 12.5$	$+11.2 \pm 1.1$
P32	GS	Dc2	4	+1.2	−6.9	$0.488 \pm 0.008$	$124.7 \pm 6.2$	$+7.1 \pm 0.7$
P4	P	Cc4	1	−1.5	−5.6	0.556	$81 \pm 21.7$	$+6.6 \pm 3.0$
P2	P	Cc5	3	−0.9	−8.6	$0.558 \pm 0.022$	$79.7 \pm 12.0$	$+3.1 \pm 1.7$
P15	S	Cc8	3	+0.7	−5.5	$0.522 \pm 0.007$	$100.78 \pm 4.2$	$+9.4 \pm 0.6$
P6	CV	Cc9	4	−1.2	−10.9	$0.521 \pm 0.008$	$101.4 \pm 5.0$	$+3.9 \pm 0.7$
P7	CV	Cc11	1	−0.8	−7.3	0.675	$30.3 \pm 13.6$	$−3.6 \pm 2.7$
P26	GS	Cc11	4	−1.4	−6.8	$0.702 \pm 0.01$	$21.6 \pm 3.0$	$−4.84 \pm 0.6$
P22	GS	Cc13	3	−0.2	−11.6	$0.617 \pm 0.017$	$52.2 \pm 7.1$	$−3.6 \pm 1.2$
P44	S	Cc15	4	−6.3	−10.3	$0.58 \pm 0.009$	$67.27 \pm 4.8$	$−0.33 \pm 0.8$

Note: n represents the number of analyses per sample.

Dc1 and Dc2 and calcite cements Cc3, Cc5, Cc8, Cc9, Cc11, Cc13, Cc14 and Cc15 have been analysed. The results are listed in Table S3 and normalized values to the Post-Archean Australian Shale (PAAS) from McLennan

(1989) are displayed in Figure 13a,b and in Table S4. Overall, the patterns for Dc1, Dc2, Rd1 and Rd2 are bell-shaped to almost flat, similar to the near-shore margin seawater reported by Deng et al. (2017) (Figure 13c). For

TABLE 5 Minimum and maximum  $^{87}\text{Sr}/^{86}\text{Sr}$  ratios of the carbonate host rocks and dolomite and calcite cements precipitated in the Upper Pedraforca thrust sheet

Description	<i>n</i>	$^{87}\text{Sr}/^{86}\text{Sr}_{\text{min}}$	$^{87}\text{Sr}/^{86}\text{Sr}_{\text{max}}$
Rd1	1	0.707816	–
Rd2	2	0.707366	0.707604
Lower Jurassic limestones	1	0.708301	–
Upper Jurassic limestones	1	0.707343	–
Upper Cretaceous limestones	3	0.707526	0.708084
S1	3	0.707747	0.707951
Dc1	1	0.707425	–
Dc2	2	0.708262	0.708354
Cc2	1	0.707857	–
Cc3	1	0.707720	–
Cc4	2	0.707563	0.707778
Cc5	1	0.707707	–
Cc8	1	0.707829	–
Cc9	1	0.709747	–
Cc11	2	0.707829	0.707919
Cc13	1	0.708855	–
Cc14	1	0.707933	–
Cc15	1	0.707751	–

Note: *n* represents the number of analyses per sample.

Rd1 the pattern shows positive Gd and Y anomalies. In contrast, patterns for Rd2 are almost flat (Figure 13a). For Dc1, this pattern shows a positive Gd anomaly, whereas for Dc2 there is a slight increase in Eu and Y anomalies. For S1, Cc3 and Cc15 the REE+Y patterns show well-defined negative Ce anomalies, whereas for Cc8, Cc9, Cc11 and Cc14 do not occur. Patterns also reveal well-defined positive Eu anomalies for Cc8, Cc9 and one S1 sample. Finally, whereas there are positive Y anomalies for Upper Cretaceous limestones, S1, Cc3, Cc8, Cc9, Cc11 and Cc15, this anomaly is absent for one sample of Cc11 and for Cc14 (Figure 13b).

The Pr/Pr\* and Ce/Ce\* ratios were calculated following the formulas of Bau and Dulski (1996) and Lawrence et al. (2006), respectively (Figure 10d,e; Table S5):

$$\text{Pr/Pr}^* = \frac{[\text{Pr}]_{\text{SN}}}{(0.5 * [\text{Ce}]_{\text{SN}})^2 + 0.5 * [\text{Nd}]_{\text{SN}}}$$

$$\text{Ce/Ce}^* = \frac{[\text{Ce}]_{\text{SN}}}{([\text{Pr}]_{\text{SN}})^2 / [\text{Nd}]_{\text{SN}}}$$

Calculations show positive La anomalies and an absence of Ce anomalies for Rd1, Rd2 and Dc2, although one

sample of Rd2 shows a positive Ce anomaly (Figure 13d). In contrast, for Dc1, a negative Ce anomaly is identified (Figure 13d). For Upper Cretaceous limestones, S1, Cc9, Cc14 and Cc15, positive La anomalies are identified, whereas Cc3, Cc8, Cc11 and Cc13 have negative Ce anomalies (Figure 13e). Calculated Y/Ho ratios (Table S5) do not show a clear trend from Rd1 to Rd2, with intermediate values between the composition of modern seawater and terrigenous sediments (Figure 13f). However, from Cc3 to Cc15, there is a progressive decrease of this ratio, from values similar to modern seawater composition to values similar to terrigenous sediments (Figure 13g).

## 5 | DISCUSSION

### 5.1 | Timing of fracturing from extension to compression

Crosscutting relationships between fracture sets coupled with U-Pb ages of calcite cements from Cruset, Vergés, et al. (2020) allow the definition of the complete sequence of deformation within the Upper Pedraforca thrust sheet (Figure 14). At the Gósol syncline (Figure 3), the en-échelon veins F1, filled with Dc1, are perpendicular to bedding and restricted to the top of the Upper Jurassic Rd1 dolostones, indicating that they formed prior to the early folding of the Jurassic rocks. Fracture system F1 is sub-orthogonal to the axis of the Gósol syncline (Figure 14), whereas the strike of F3 fractures is parallel to the axis of this fold. Jurassic rocks hosting these fractures are unconformably overlain by Lower Cretaceous sedimentary breccias, which are composed of fragments of Jurassic limestones and dolostones including reworked fragments of F1 veins filled with Dc1 and F3 veins filled with Dc2 (Figure 6b). This indicates that F1 and F3 veins, and consequently F2 veins, formed before Lower Cretaceous sedimentary breccia deposition. Furthermore, after restoring the Gósol syncline to an orientation prior to the Pyrenean compression, F1 and F3 exclusively concentrate in the vicinity of the overturned SE limb. The array of these fractures fits well with those documented in diapiric provinces worldwide (Coleman et al., 2018; Fischer et al., 2013; Smith et al., 2012), where fractures perpendicular and subparallel to salt walls are concentrated in the vicinity of salt welds. Therefore, F1 and F3 veins are interpreted to have formed along the walls of diapirs. Within this diapiric setting, at the Gósol locality, Lower Cretaceous breccias with metre-scale blocks of Jurassic limestones and dolostones could reflect the collapse of carbonate platforms during rise of active diapirs. This agrees with Saura et al. (2016), who interpreted that the north Pyrenean margin of Iberia, including the Upper



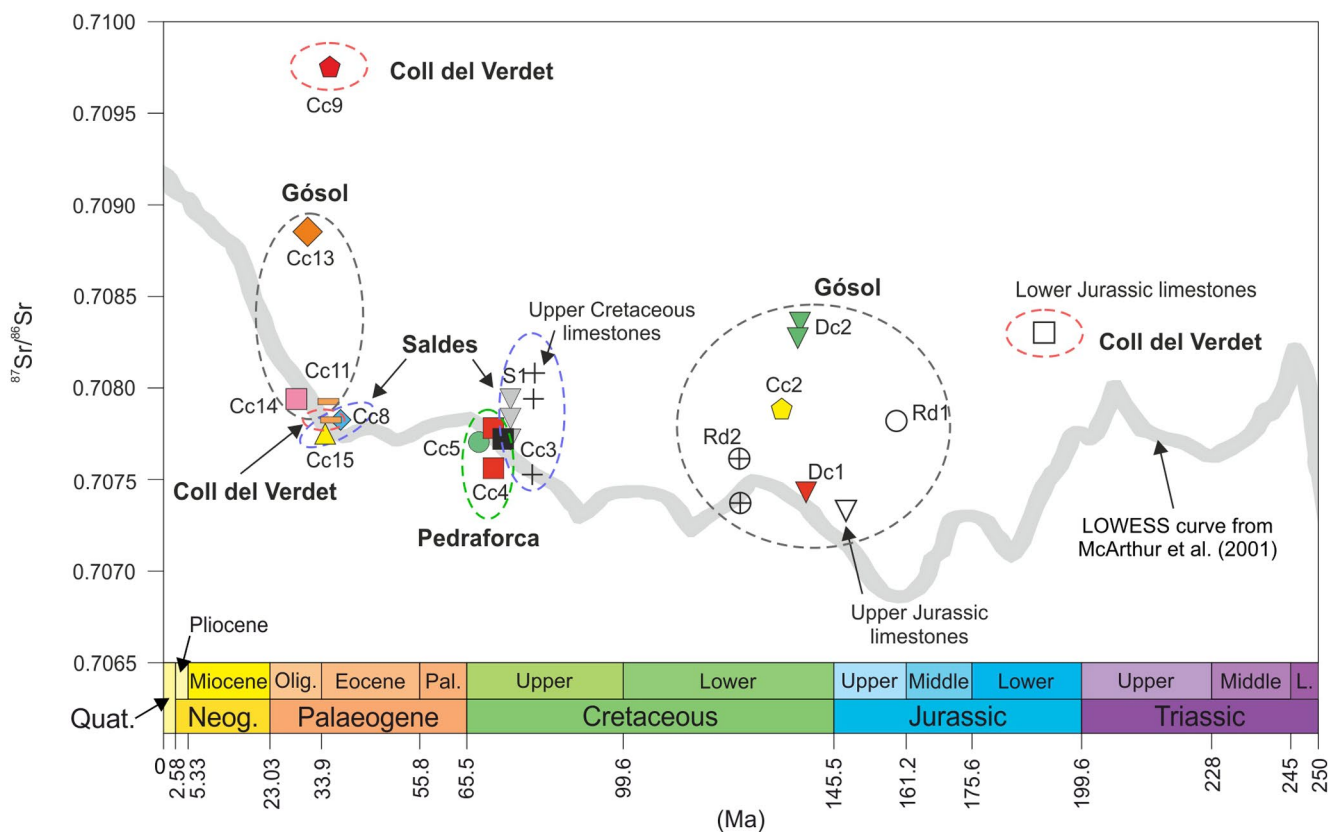


**FIGURE 12**  $^{87}\text{Sr}/^{86}\text{Sr}$  composition of dolomite and calcite cements, and carbonate host rocks from the Upper Pedraforca thrust sheet. The ages for each type of cement are based on relative crosscutting relationships between fracture sets, host rocks and cements dated in Cruset, Vergés, et al. (2020). The LOWESS curve from McArthur et al. (2001) is also plotted. Symbols for each cement are the same than in Figures 11, 13 and 14. Reference colours for each locality are the same than in Figures 3, 5, 11, 13 and 14

Pedraforca thrust sheet, acted as a salt-related margin, initiated during the Jurassic, which continued during the Early Cretaceous (also see Vergés & Garcia-Senz, 2001; García-Senz, 2002). Normal faults F4, containing Cc2, crosscut the aforementioned Lower Cretaceous breccias and therefore, we interpret that they formed during the Early Cretaceous.

Cc4 precipitated in hydraulic breccias within the damage zone of the Upper Pedraforca basal thrust and Cc5 in F5, F6, F7 and F8 yielded four U-Pb ages from  $70.6 \pm 0.9$  (early Maastrichtian) to  $55.3 \pm 0.5$  Ma (earliest Ypresian; Figure 14). These latest Cretaceous-earliest Paleocene ages indicate that F4 to F8 fractures formed during the emplacement of the Upper Pedraforca thrust sheet (Cruset, Vergés, et al., 2020; Puigdefàbregas & Souquet, 1986; Vergés et al., 2002). After their formation, the hydraulic breccias were cut by F9 veins, filled with Cc6.

Cements Cc7 to Cc11, Cc13 and Cc15 have measured U-Pb dates ranging from  $47 \pm 10.5$  (earliest Lutetian) to  $34.9 \pm 16.5$  Ma (Priabonian) (Figure 14). The U-Pb ages of these cements, and their crosscutting relationships,

indicate that fractures F9 to F15 grew, and F1 and F8 were reactivated coevally, with the emplacement of the Lower Pedraforca and Cadí thrust sheets from the early Eocene to the latest Oligocene (Burbank, Puigdefàbregas, et al., 1992; Burbank, Vergés, et al., 1992; Cruset, Vergés, et al., 2020; Grool et al., 2018; Vergés et al., 2002; Figure 14). During this period, the Upper Pedraforca thrust sheet was folded and carried out above the younger Lower Pedraforca and Cadí thrust sheets. Finally, F16 cutting F14 has a constant orientation regardless of bedding dips, probably indicating their growth during post-emplacement deformation.

## 5.2 | Fluid flow evolution linked to salt-related extension and inversion tectonics

The integration of fracture, petrographic, geochemical and geochronological data from the Upper Pedraforca thrust sheet allows the identification of four major fluid flow events, correlated with four stages of its tectonic history: (1) Late Jurassic pre-extension; (2) Early Cretaceous salt-related extension; (3) Late Cretaceous-Palaeocene

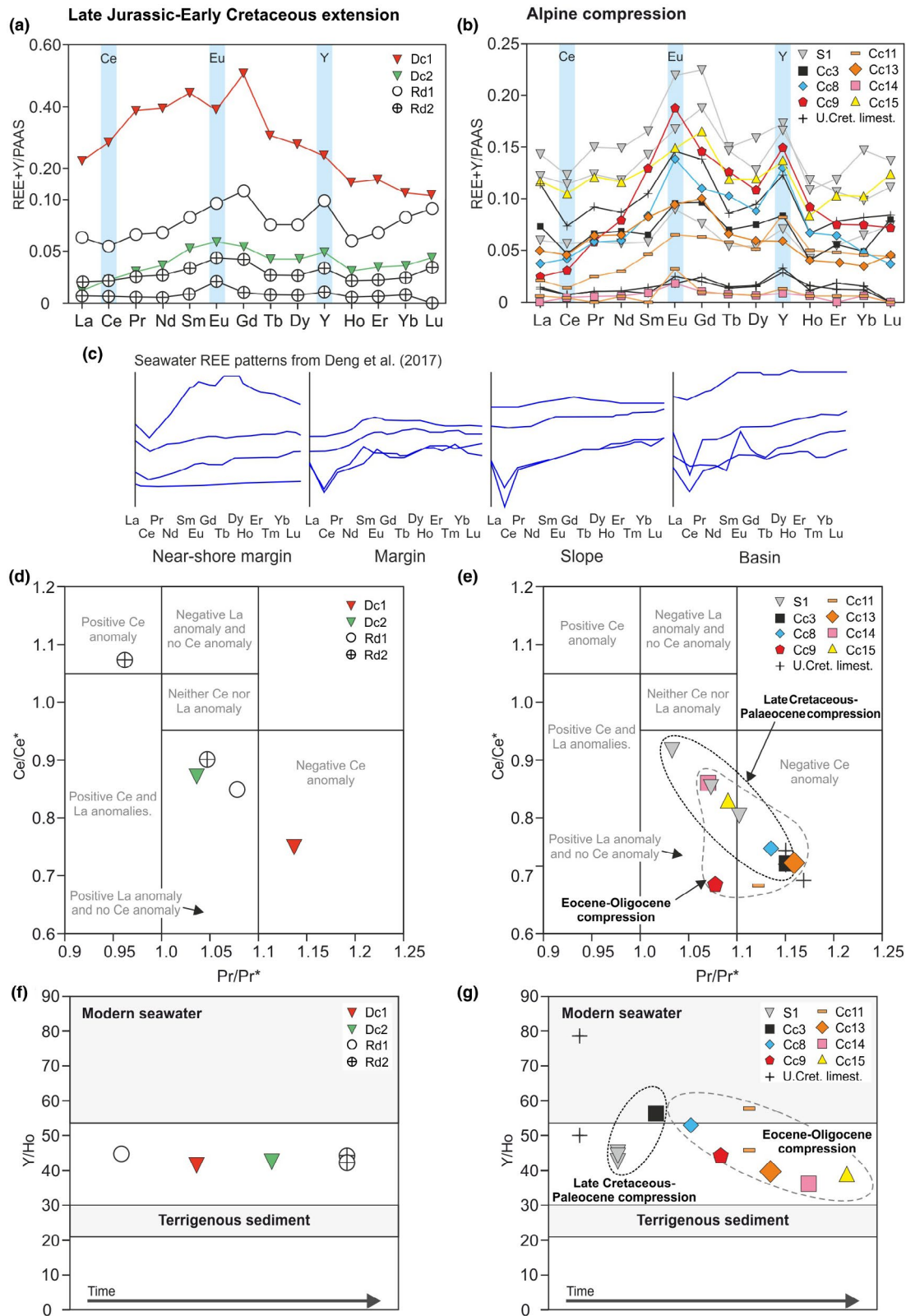


**FIGURE 13** (a, b) PAAS-normalized REE+Y distribution patterns of carbonate host rocks and calcite and dolomite cements. (c) PAAS-normalized REE patterns of Pacific Ocean seawater from Deng et al. (2017). (d, e) PAAS-normalized Ce/Ce\* versus Pr/Pr\* cross-plot to analyse the Ce and Pr anomalies of carbonate host rocks and dolomite and calcite cements. The method of Bau and Dulski (1996) modified by Webb and Kamber (2000) is used. (f, g) Y/Ho ratios of carbonate host rocks and calcite and dolomite cements. Y/Ho limits for modern seawater and terrigenous sediments are based on Bau and Dulski (1994) and Zhao et al. (2013). Symbols for each cement are the same than in Figures 11, 12, and 14



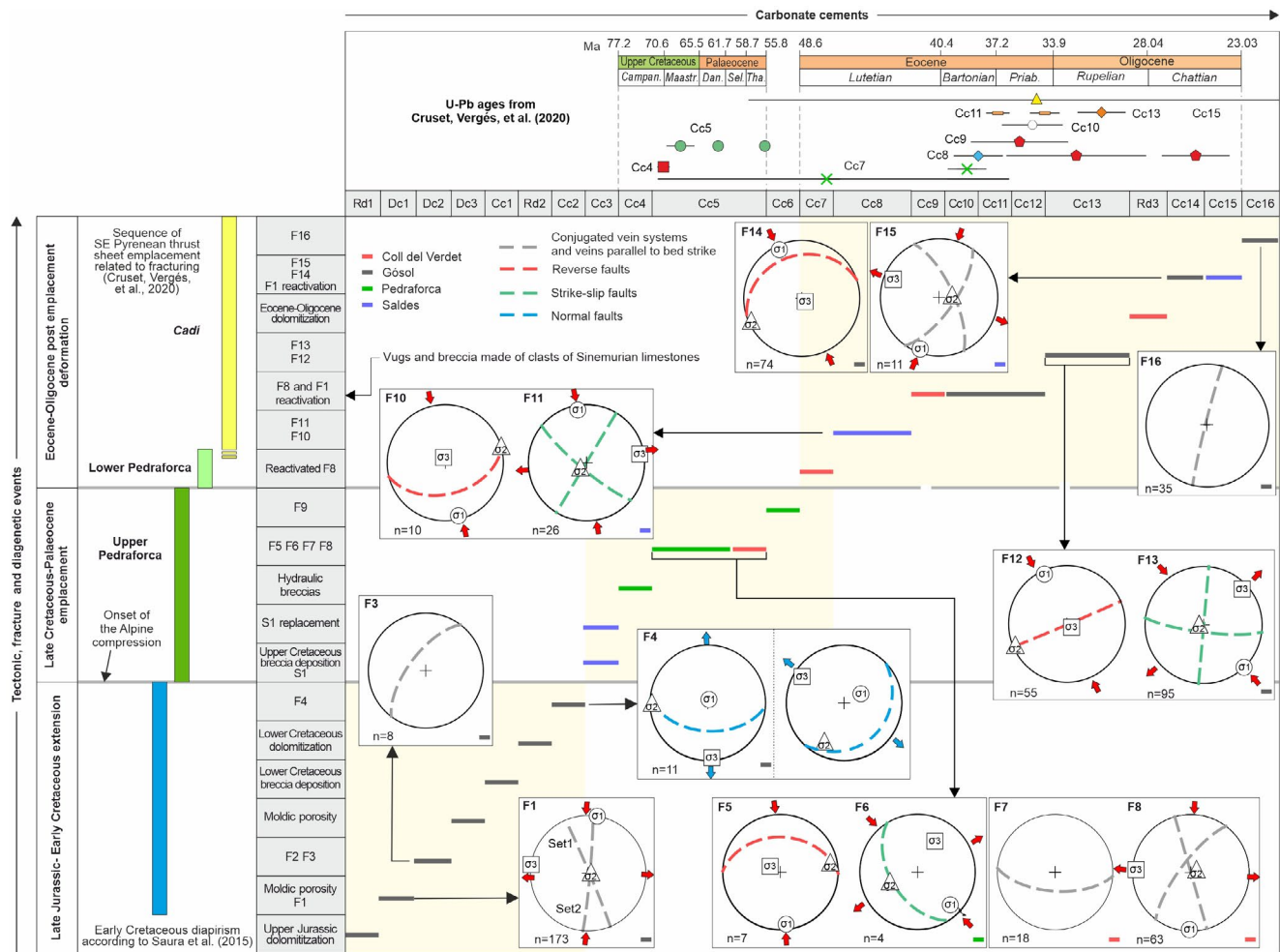


**FIGURE 14** Summary of the tectonic, fracture and diagenetic events during the evolution of the Upper Pedraforca thrust sheet. The sequence of cement precipitation is constrained with U-Pb ages from Crusset, Vergés, et al. (2020). Symbols for each U-Pb age are the same than cements in Figures 11–13. Reference colours for each locality are the same than in Figures 3, 5, 11–13. The correlation between fracture and diagenetic events with the timing of SE Pyrenean thrust sheets emplacement is based on the results of Crusset, Vergés, et al. (2020). The timing in the Early Cretaceous diapirism is based on Saura et al. (2015)

thrust sheet emplacement; and (4) Eocene-Oligocene post-emplacment deformation (Figure 15).

### 5.2.1 | Late Jurassic pre-extension

Replacive dolostones Rd1 are older than sedimentary breccias that were deposited during the Early Cretaceous. This reveals a Late Jurassic dolomitization event (Figure 15a) that is in agreement with the study of Arnal et al. (2002), who proposed that large volumes of limestones were dolomitized in the Southern Pyrenees at the end of the Jurassic. The  $\delta^{13}\text{C}$  and  $\delta^{18}\text{O}$  of Rd1 fall within the range of Jurassic-Cretaceous marine carbonates (Veizer et al., 1999) (Figure 11a). Likewise, its positive Gd and Y anomalies also reflect the influence of seawater (Figure 10a; Tostevin et al., 2016). However, the  $^{87}\text{Sr}/^{86}\text{Sr}$  ratio of Rd1, much higher than

that of Late Jurassic seawater (Figure 9), could indicate a significant influence of siliciclastic sediment (e.g. detrital phyllosilicates and feldspars), also reflected by the absence of negative cerium anomalies and by the Y/Ho ratios (Tostevin et al., 2016) (Figure 13c,e). The REE+Y pattern of Rd1, similar to that of near-shore margin seawaters (Deng et al., 2017), suggests dolomitization in a coastal setting with terrigenous inputs. Furthermore, the absence of marked Eu anomalies for Rd1 (Figure 10a) suggests that this replacive dolomite grew from fluids at low temperatures (Bau & Dulski, 1996; Tostevin et al., 2016). Therefore, we interpret that replacive dolomite Rd1 could result from the migration of Mg-enriched seawater that interacted with siliciclastic sediments in a shallow burial environment. The source of magnesium could be the underlying Toarcian marine marls and/or the Upper Triassic evaporites (Figure 2).

## 5.2.2 | Early Cretaceous salt-related extension

During Early Cretaceous diapirism, high-temperature formation waters migrated through fractures F1, F2 and F3 (Figure 15b,c), as attested by the clumped isotope temperatures in dolomite cements ( $149.4 \pm 12.5^\circ\text{C}$  for Dc1 and  $124.7 \pm 6.2^\circ\text{C}$  for Dc2) and  $\delta^{18}\text{O}_{\text{fluid}}$  ( $+11.2 \pm 1.1\text{‰}$  VSMOW for Dc1 and  $+7.1 \pm 0.7\text{‰}$  VSMOW for Dc2; Figure 11b). For Dc1, the high  $\delta^{18}\text{O}_{\text{fluid}}$ , temperature and  $^{87}\text{Sr}/^{86}\text{Sr}$  ratio of 0.707816 could indicate that this dolomite precipitated from evolved Early Cretaceous seawater heated at depth, as also evidenced by its Gd positive anomaly and negative Ce anomaly (Bau & Dulski, 1996; Lécuyer et al., 2004; Tostevin et al., 2016; Figures 9 and 10a,c). Alternatively, the high  $\delta^{18}\text{O}_{\text{fluid}}$  of Dc1 is also compatible with saline fluids derived from Upper Triassic evaporites, which could have mixed with Early Cretaceous seawater. This potential mixing between evaporitic brines and seawater has been identified in fracture-filling cements from the Northern Pyrenees, where Upper Triassic evaporites were involved in salt-related extension (Cathelineau et al., 2021). This tectonic and fluid-flow scenario could fit with that of the Upper Pedraforca thrust sheet during the Early Cretaceous. For Dc2, the absence of negative Ce anomalies indicates the presence of reducing fluids (Lécuyer et al., 2004; Tostevin et al., 2016), whereas the high  $^{87}\text{Sr}/^{86}\text{Sr}$  ratios, from 0.708262 to 0.708354, measured in this cement are interpreted as the input of formation waters that previously interacted with highly radiogenic rocks. A potential source for these fluids could be underlying pre-salt rocks (e.g. crystalline basement rocks or its sedimentary cover constituted by the Early Triassic Buntsandstein siliciclastics), which were probably in contact with Pyrenean post-salt carbonate successions during development of primary welds (Figure 15c). Similar patterns of fluid migration have also been documented in other extensional settings of the Alpine domain. As an example, in the Chaînons Béarnais of the northwestern Pyrenees, primary welding favoured the ascent of basement-derived fluids to post-salt carbonate rocks (Motte et al., 2021). Similarly, the development of extensional detachments in the Err Nappe of the Swiss Alps favoured brecciation of carbonate units directly in contact with crystalline basement rocks, which facilitated the upward migration of high-temperature fluids with high  $^{87}\text{Sr}/^{86}\text{Sr}$  ratios (Incerpi et al., 2017).

At the Gósol locality, the Lower Cretaceous sedimentary breccias, cemented by Cc1, are characterized by depleted  $\delta^{18}\text{O}$  values between  $-10.6$  and  $-7.9\text{‰}$  VPDB, which can be attributed to precipitation from both high-temperature formation waters or low-temperature meteoric fluids (e.g. Cerling & Quade, 1993; Emery, 1987; Lacroix et al., 2018; Veizer & Hoefs, 1976). Subsequently,

calcite Cc2 precipitated in F4 normal faults cutting the breccias. This cement presents depleted  $\delta^{18}\text{O}$  values between  $-12.26$  and  $-9.20\text{‰}$  VPDB, which can be attributed to: (1) fluids with temperatures higher than those of Cc1; or (2) the mixing between the fluid from which Cc1 precipitated and a more  $\delta^{18}\text{O}$ -depleted one (Cruset et al., 2018; Emery, 1987; Hausegger et al., 2010; Immenhauser et al., 2007). The high  $^{87}\text{Sr}/^{86}\text{Sr}$  ratios of Cc2 indicate that fluids probably interacted with siliciclastic sediments within the Lower Cretaceous breccias, which were unconformably overlain by thick Lower Cretaceous carbonate platforms during the same period (Figures 2 and 3a).

At the bottom of the Lower Cretaceous carbonate platforms, 30 cm-thick tabular limestones were replaced by dolomite Rd2 (Figure 15d), with  $\delta^{13}\text{C}$  and  $\delta^{18}\text{O}$  values close to the composition of Jurassic-Cretaceous marine carbonates (Veizer et al., 1999) (Figure 11a). The  $^{87}\text{Sr}/^{86}\text{Sr}$  ratio of Rd2 is also within the range of Early Cretaceous seawater (Figure 12), although the absence of negative cerium anomalies and the Y/Ho ratios also accounts for the influence of siliciclastic sediments (Tostevin et al., 2016). The absence of positive Eu anomalies in Rd2 suggests that this dolomite precipitated from fluids with a low temperature (Bau & Dulski, 1996; Tostevin et al., 2016). Therefore, like Rd1, the origin of Rd2 might also be related to low-temperature Mg-rich seawater that interacted with siliciclastic sediments. The origin of Rd2 dolomite is thus different from that of the rift-related replacive dolostones from the Chaînons Béarnais in the North Pyrenean Zone, which could be the product of the migration of deep and hot Mg-rich fluids through fractures during Early Cretaceous rifting, according to Salardon et al. (2017) and Motte et al. (2021).

## 5.2.3 | Late Cretaceous-Palaeocene thrust sheet emplacement

Syn-tectonic sedimentary breccias, coevally with the interparticle micrite sediment S1, were deposited at the front of the Upper Pedraforca thrust sheet (Figure 15e). The depleted  $\delta^{18}\text{O}$  values of sediment S1 with respect to Late Cretaceous marine carbonates could indicate that S1 was probably sourced from limestones affected by burial diagenesis (Emery, 1987) (Figure 11a). The absence of negative Ce anomalies for S1, its low Y/Ho ratios and its high  $^{87}\text{Sr}/^{86}\text{Sr}$  ratios can be interpreted as the influence of siliciclastic sediments (Figures 12 and 13d), whereas the positive Y anomaly possibly reflects the influence of seawater. The  $\delta^{13}\text{C}$  and  $\delta^{18}\text{O}$ ,  $^{87}\text{Sr}/^{86}\text{Sr}$ , Y positive anomaly and Y/Ho ratio of Cc3 indicate that the replacement of S1 by this cement was due to circulation of seawater or fluids interacting with marine carbonates (Figures 11a, 12 and 13).



Cements Cc4 to Cc6 precipitated within hydraulic breccias and in fractures F5 to F9 within the basal thrust fault zone and the internal part of the Upper Pedraforca thrust sheet (Pedraforca and Coll del Verdet localities). Clumped isotope thermometry applied to Cc4 and Cc5 yielded  $\delta^{18}\text{O}_{\text{fluid}}$  values of  $+6.6 \pm 3\%$  and  $+3.1 \pm 1.7\%$  VSMOW, respectively, and temperatures of around  $80^\circ\text{C}$  (Figure 11b), indicating that these cements precipitated from formation waters (Taylor, 1987). The  $^{87}\text{Sr}/^{86}\text{Sr}$  ratios of Cc4 and Cc5 reveal both Upper Triassic and Late Cretaceous seawater signatures (between 0.707563 and 0.707778) (Figure 12), possibly indicating that these cements precipitated from: (1) evolved seawater, (2) remobilized fluids from the Upper Triassic evaporites interacting with Late Cretaceous carbonates or (3) a combination of both possibilities. A seawater influence has been demonstrated in the western equivalent unit, the Bóixols thrust sheet (Nardini et al., 2019), where lower  $\delta^{18}\text{O}_{\text{fluid}}$  values of  $+0.6$  to  $+1.6\%$  VSMOW have been calculated in cements precipitated within strike-slip faults cutting the Bóixols anticline (Figure 11b). However, the cements studied by the previous authors are not equivalent with those of this study. Additionally, the strike-slip faults in the Bóixols anticline crosscut its forelimb and footwall, whereas Cc4 and Cc5 cements in the Upper Pedraforca thrust sheet precipitated in fractures along its basal thrust, which is detached in Upper Triassic evaporites. Different studies along the Pyrenees have suggested that fluids derived from Upper Triassic evaporites that acted as main thrust sheet detachments during the Alpine compression were probably remobilized (e.g. Cathelineau et al., 2021; Crognier et al., 2018; Cruset, Cantarero, et al., 2020). This scenario is compatible with the high  $\delta^{18}\text{O}_{\text{fluid}}$  values of Cc4 and Cc5 precipitated in the Upper Pedraforca basal thrust. The decrease of these values from Cc4 to Cc5 could be attributed to the input of meteoric fluids into the system, as has been already reported in other areas in the SE Pyrenees. These areas include the Vallfogona thrust carrying the Cadí thrust sheet (Cruset et al., 2018), the Jaca thrust in the southwestern Pyrenees (Lacroix et al., 2014), the Puig-reig anticline in the foreland Ebro basin (Cruset et al., 2016) and possibly in the Cotiella thrust in the Aínsa basin (Travé et al., 1997). This scenario is supported by the fossilization of the Upper Pedraforca thrust sheet by Late Cretaceous to Palaeocene non-marine syn-orogenic red beds (Figure 3), indicating its frontal emersion and facilitating the percolation of meteoric waters (Figure 15e). After Cc4 calcite precipitation, during development of F9, Cc6 precipitated with a  $\delta^{18}\text{O}$  of  $-6.1\%$  VPDB, a value slightly depleted with respect to the Mesozoic marine carbonates (Veizer et al., 1999; Figure 11a). These depleted values suggest precipitation from hotter fluids or from low-temperature meteoric waters. In both cases, the  $\delta^{13}\text{C}$  values of Cc6 between  $-1.42$  and  $-1.10\%$  VPDB, suggest the

influence of seawater or the interaction of the fluid from which this cement precipitated with marine carbonates (Figure 11a).

Burial depths can be estimated from the temperatures of  $81 \pm 21.7$  and  $79.7 \pm 12.0^\circ\text{C}$  measured for Cc4 and Cc5 in the Upper Pedraforca thrust sheet, considering the likely geothermal gradients during the Late Cretaceous to Palaeocene compression. In the southern Pyrenees, geothermal gradients between  $25$  and  $35^\circ\text{C}/\text{km}$  have been estimated for the Alpine compression period using thermochronology modelling of granodiorite samples from the Axial Zone as well as vitrinite reflectance and Raman spectroscopy applied to carbonaceous materials in Eocene turbidites (Labaume et al., 2016; Metcalf et al., 2009). These values are similar to slightly higher than the  $25^\circ\text{C}/\text{km}$  typical of foreland basins and the present-day  $22.6^\circ\text{C}/\text{km}$  in the detached southern Pyrenees (Allen & Allen, 2013; Fernández et al., 1998). Considering these gradients as constant during the whole Pyrenean compression, and the temperatures of around  $80^\circ\text{C}$  measured in Cc4 and Cc5, burial depths between  $3.2$  and  $2.3$  km are thus estimated. These depths are within the range of ca.  $2.5$  km estimated for the thickness of the Upper Pedraforca thrust sheet, according to the cross-sections of García-Senz (2002) and could indicate that fluid temperatures in this thrust sheet were likely reached by burial.

#### 5.2.4 | Eocene-Oligocene post-emplacement deformation

Post-emplacement deformation within the Upper Pedraforca thrust sheet was characterized by a highly heterogeneous fluid system, with different types of fluids migrating through fractures at different structural positions (Figure 15f). The  $\delta^{18}\text{O}_{\text{fluid}}$  of Cc8 and Cc9 in the basal thrust fault zone (Salades locality) follows the same decreasing trend than Cc4 and Cc5 during the Late Cretaceous-Palaeocene emplacement ( $103.3 \pm 5.5^\circ\text{C}$  and  $+9.8 \pm 0.8\%$  VSMOW for Cc8 and  $101.4 \pm 5^\circ\text{C}$  and  $+3.9 \pm 0.7\%$  VSMOW for Cc9) (Figure 11a,b). These  $\delta^{18}\text{O}$  values and temperatures record again the migration of formation waters, which probably interacted with Upper Triassic evaporites, and that progressively mixed with meteoric fluids. This similarity suggests that during both periods, the same type of fluid migrated through the same area with a difference of tens of millions of years ( $70.6 \pm 0.9$  to  $55.3 \pm 0.5$  Ma for Cc4 and Cc5 and  $38.2 \pm 1.4$  Ma, to  $25.7 \pm 1.9$  Ma for Cc8 and Cc9). The positive Y anomalies for Cc8 and Cc9 also suggest the influence of marine fluids or the interaction of formation waters with marine host-rocks.

Different types of fluids (from which Cc7 and Cc10 to Cc16 precipitated) migrated in the internal part, at shallower

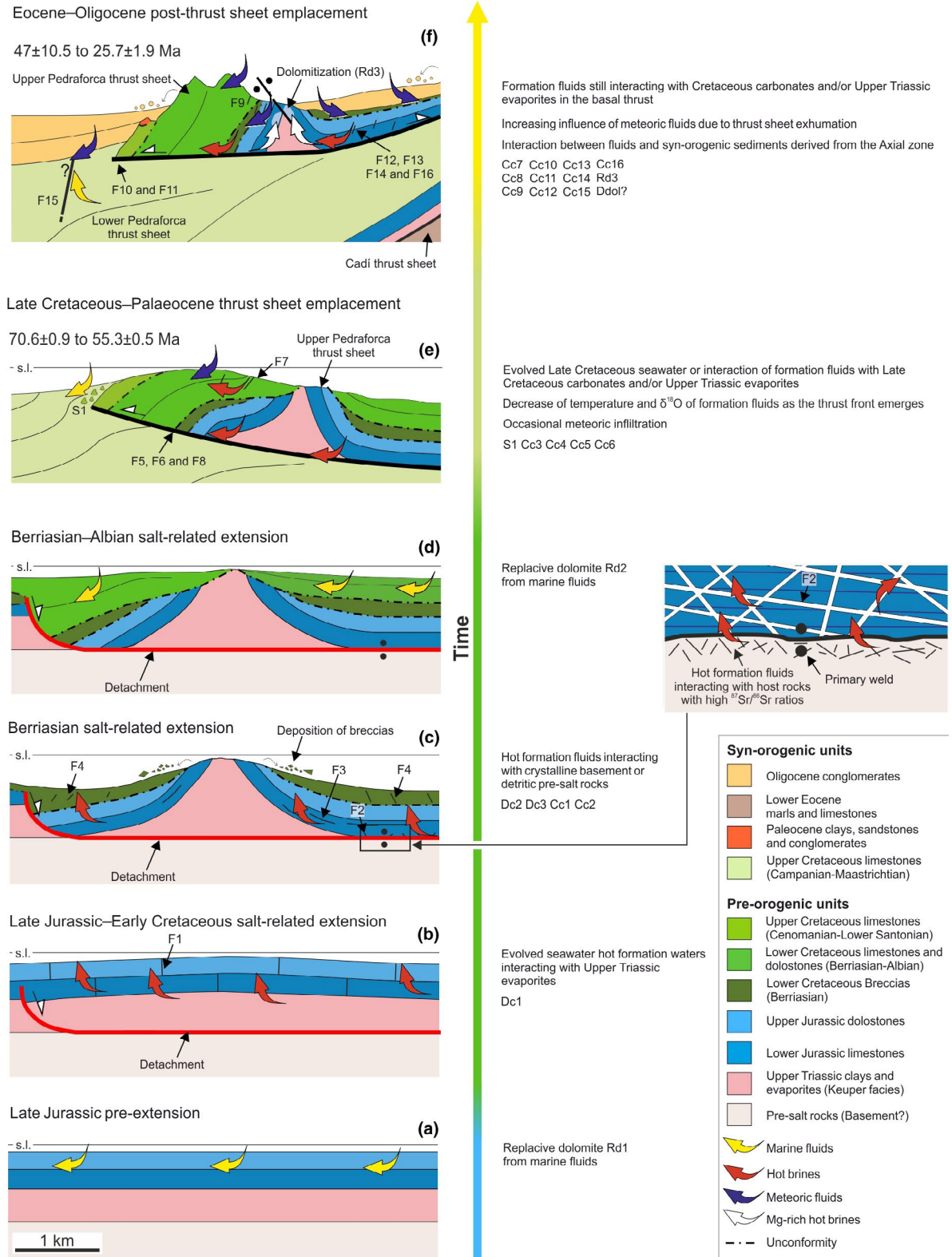


FIGURE 15 Fluid flow evolution in the Upper Pedraforca thrust sheet from the Late Jurassic to the Oligocene

positions and at the footwall of the Upper Pedraforca thrust sheet, in contrast with the homogeneous fluid system that characterizes the basal thrust fault zone (Cc8 and Cc9). Cc11

cementing Sinemurian-derived breccias and centimetre-size vugs within Rd1 dolostones in Coll del Verdet and Gósol localities, as well as calcite cement Cc13 precipitated in F12



and F13 fractures, have clumped isotopes temperatures between  $23.3 \pm 2.3^\circ\text{C}$  and  $52.2 \pm 7.1^\circ\text{C}$  and  $\delta^{18}\text{O}_{\text{fluid}}$  values between  $-4.5 \pm 0.5\text{‰}$  and  $-3.6 \pm 2.7\text{‰}$  VSMOW, respectively, indicating precipitation from low-temperature meteoric waters. Likewise, calcitized dolomite present at the Gósol and Coll del Verdet localities (Ddol) also indicates alteration of dolomite by these fluids. The  $\delta^{13}\text{C}$  and  $\delta^{18}\text{O}$  compositions of Cc7, Cc12 and Cc16 from  $-9.39$  to  $-1.08\text{‰}$  VPDB for  $\delta^{13}\text{C}$  and from  $-9.17$  to  $-5.47\text{‰}$  VPDB for  $\delta^{18}\text{O}$  (Figure 11), are similar to carbonates with meteoric signature, according to the measurements of Veizer and Hoefs (1976). Furthermore, the low  $\delta^{13}\text{C}$  values of these cements also could indicate the input of soil-derived  $\text{CO}_2$  (Cerling & Quade, 1993; Jolivet & Boulvais, 2021). The increasing meteoric influence in calcite cements Cc7, Cc11, Cc12, Cc13, Cc16 and Ddol, with respect to those precipitated during the Late Cretaceous-Palaeocene thrust emplacement, could be related to the progressive exhumation of the Pyrenees from the Late Eocene to the Oligocene due to the emplacement of the Cadí thrust sheet and the end of marine conditions in the southern Pyrenees at 36 Ma (Costa et al., 2010; Serra-Kiel, Mató, et al., 2003; Serra-Kiel, Travé, et al., 2003). This exhumation is also attested by the progressive decrease of the Y/Ho ratios from Cc8 to Cc15 (from 52.87 to 38.31; Figure 13), accounting for an increasing influence of siliciclastic sediments (Tostevin et al., 2016). Erosion of the Pyrenean Axial Zone during the Late Eocene-Oligocene could be the potential source for these sediments, which buried the adjacent south Pyrenean thrust sheets (Beamud et al., 2003; Fillon et al., 2013). This additional burial could be responsible for the slight increase of fluid temperatures measured in Cc8 and Cc9 during the Eocene-Oligocene (ca.  $100^\circ\text{C}$ ) with respect to that in Cc4 and Cc5 during the Late Cretaceous-Palaeocene (ca.  $80^\circ\text{C}$ ). The high  $^{87}\text{Sr}/^{86}\text{Sr}$  ratios between 0.708855 and 0.709747 of Cc9 and Cc13 support the increasing influence of siliciclastic sediments derived from igneous and metamorphic rocks of the Pyrenean Axial Zone, which have ratios between 0.708653 and 0.754132 (Banks et al., 1991; Bickle et al., 1988; McCaig et al., 1995; Muñoz-López, Alías, et al., 2020). On the other hand, the  $^{87}\text{Sr}/^{86}\text{Sr}$  ratios of cements Cc8, Cc11 and Cc14 (0.707829 to 0.707933) fall within the range of Early Jurassic and Late Cretaceous seawater (0.707077 to 0.707833), indicating high interaction of the meteoric waters with host marine carbonates (Figure 12).

Below the Upper Pedraforca basal thrust, the measured clumped isotope temperature of Cc15 precipitated in F15 at the Saldes locality is  $68.8 \pm 4.4^\circ\text{C}$  and the  $\delta^{18}\text{O}_{\text{fluid}}$  of  $-0.1 \pm 0.7\text{‰}$  VSMOW. These values suggest precipitation from marine fluids or evolved meteoric waters, as attest the low  $\delta^{13}\text{C}$  values between  $-6.2$  and  $-4.29\text{‰}$  VPDB of Cc15. The  $^{87}\text{Sr}/^{86}\text{Sr}$  ratio (0.707751) and positive Y anomaly of this cement could also indicate the influence of Late Cretaceous marine seawater trapped within host sediment

pores or interaction of fluids with Late Cretaceous marine host rocks (Figures 12 and 13).

Finally, Rd3 dolomite exhibits saddle textures, indicating temperatures of precipitation between 60 and  $>250^\circ\text{C}$  (Gregg & Sibley, 1984; Motte et al., 2021; Sibley & Gregg, 1987; Sijing et al., 2014). This dolomite replaces carbonate breccias made of fragments of Sinemurian limestones and cement Cc11 with U-Pb ages from  $37.1 \pm 0.7$  Ma to  $34.4 \pm 0.9$  Ma at the vicinity of the Coll del Verdet, which has been interpreted as a secondary weld zone by Saura et al. (2016). The relative age and the saddle texture of Rd3 indicate that this dolomite could have formed from hot Mg-rich fluids migrating along diapir walls during the Eocene compression (Figure 15f). Considering that marine conditions in the Pyrenean foreland basin ended around 36 Ma (Costa et al., 2010; Serra-Kiel, Mató, et al., 2003; Serra-Kiel, Travé, et al., 2003), the influence of marine fluids during precipitation of Rd3 is ruled out. An alternative hypothesis is the upward migration of dolomitizing fluids along the diapir walls (e.g. Masoumi et al., 2014; Moragas et al., 2020; Smith et al., 2012), which could result from their expulsion due to compaction of deep Toarcian and/or Keuper marls during shortening (Figure 15f). The limited volume of host rock replaced by Rd3 agrees with a sediment compaction mechanism for dolomitizing fluid expulsion (Bitzer et al., 2001; Gomez-Rivas, Corbella, et al., 2014; Machel, 2004; Warren, 2000). The influence of meteoric waters and the absence of Rd3 away from the diapir walls indicate that the Coll el Verdet secondary weld acted as the preferential conduit for dolomitizing fluids. This behaviour has also been documented in other diapiric areas worldwide, such as the La Popa basin in Mexico (Smith et al., 2012) and the High Atlas in Morocco (Moragas et al., 2020).

### 5.3 | Fluids and mineralization in diapiric domains

The studies of Saura et al. (2016), López-Mir et al. (2015), Hudec et al. (2021) and Burrel and Teixell (2021) described the influence of salt-related diapirism on the southern Pyrenees structure. The diapiric structure of the Pyrenees presents some similarities with that of other areas such as the Basque-Cantabrian Zone (Perona et al., 2018), the Central High Atlas in Morocco (Mouttaqi et al., 2011), the Tunisia Salt Diapir Province (Bouhleb et al., 2016; Sheppard et al., 1996) and the Hormuzgan Province of Iran (Hassanlouei & Rajabzadeh, 2019), among others. In these diapiric domains, replacive dolomite, cap rocks and veins all host Zn-Pb mineralization related to the migration of hot brines that interacted with organic matter.

The palaeofluid evolution of the Upper Pedraforca thrust sheet, which is well-constrained by geochronological

and geochemical analytical methods, provides insights into the spatial and temporal distribution of mineralization and supergene processes along similar inverted salt-related structures that could be targets for mining exploration. As an example, meteoric percolation occurred in the Upper Pedraforca thrust sheet in vug porosity, between breccia clasts, in calcitized dolostones as well as along fracture sets that newly formed during the Alpine compression (Figure 15e,f). This spatial and temporal distribution of fluids suggests that the increasing meteoric influence during the rise of diapiric structures in areas with similar settings as those of the Upper Pedraforca may enhance ore weathering and the development of supergene deposits (e.g. Hassanlouei & Rajabzadeh, 2019). This scenario is documented in Zn-Pb mineralization hosted in diapirs in northern Tunisia and the Hormuzgan province in the Zagros, where supergene deposits formed due to weathering of salt bodies during the Alpine compression (Garnit et al., 2018; Hassanlouei & Rajabzadeh, 2019). In contrast, in the Murguía diapir in the Basque-Cantabrian Basin (Ábalos et al., 2003; Stackelberg, 1960), supergene mineralization was not identified (Perona et al., 2018). According to these authors, Zn-Pb mineralization in the Murguía diapir formed before the Campanian stage, probably before the Pyrenean compression in this particular diapiric structure.

The development of fracture set F2 cutting the basal part of Jurassic successions of the Upper Pedraforca thrust sheet facilitated the upward migration of hot fluids that interacted with pre-salt rocks with high  $^{87}\text{Sr}/^{86}\text{Sr}$  ratios (Buntsandstein siliciclastics and/or the Palaeozoic basement). The transfer of fluids from crystalline pre-salt rocks to shallower positions in similar settings could create the ideal conditions for ore accumulations in post-salt carbonates, as is the case of the brecciated detachment zones in the Carboniferous carbonates of the Windsor Group in the Maritimes basin of Canada (Lynch et al., 1998). The relationship between fluid flow and brecciation of carbonate rocks in contact with crystalline basement rocks may open new strategies of exploration in outcropping areas such as the extensional detachments of the Swiss Alps, where fluids derived from the Palaeozoic basement also migrated to brecciated Upper Triassic and Lower Jurassic carbonates (Incerpi et al., 2017). The Schwarzwald mining district in southwest Germany also contains key examples of Jurassic unconformity-related hydrothermal ore deposits, involving hot basement-derived brine circulation, fracturing and brecciation (e.g. Bons et al., 2014).

## 6 | CONCLUSIONS

The complex paleohydrological history of the Upper Pedraforca thrust sheet in the SE Pyrenees has here been

unravelling from the combined study of fracture orientations, and petrographic, geochemical and geochronological analyses, leading to the following conclusions:

1. Mg-rich low-temperature seawater caused the dolomitization of thick Jurassic and Lower Cretaceous carbonate units at shallow burial conditions during Late Jurassic and Early Cretaceous extensional events.
2. During the Early Cretaceous salt-related extension, formation waters, which were probably seawater mixed with brines that were derived from Upper Triassic evaporites, migrated through fractures related to diapiric growth. These fluids had temperatures of around 150°C and a  $^{87}\text{Sr}/^{86}\text{Sr}$  ratio of 0.707425.
3. Fractures formed in the Jurassic rocks, due to primary salt welding, facilitated the migration of formation fluids at temperatures of 125°C that interacted with pre-salt rocks with high  $^{87}\text{Sr}/^{86}\text{Sr}$  ratios between 0.708262 and 0.708354 (Buntsandstein siliciclastics or crystalline basement rocks).
4. Normal faults, cutting sedimentary breccias related to the collapse of carbonate platforms during diapir growth, acted as conduits for hot fluids.
5. Formation waters at ca. 80°C migrated through the whole Upper Pedraforca thrust sheet during the Late Cretaceous to Palaeocene thrust sheet emplacement, although local inputs of meteoric fluids also occurred. The geochemical composition of fracture-filling cements could indicate that fluids interacted with Upper Triassic evaporites or evolved Late Cretaceous seawater with  $^{87}\text{Sr}/^{86}\text{Sr}$  ratios between 0.707563 and 0.707778.
6. Along the basal thrust fault zone, the fluid regime during the Eocene to Oligocene post-emplacement deformation was similar to that during the Late Cretaceous-Palaeocene emplacement, with formation waters at temperatures of ca. 100°C and  $\delta^{18}\text{O}_{\text{fluid}}$  values between +3.9 and +9.8‰ VSMOW.
7. In the Upper Pedraforca unit, the influence of both low-temperature meteoric fluids and siliciclastic sediments derived from the Axial Zone covering the thrust sheet increased with respect to the Late Cretaceous-Palaeocene, recording the exhumation of the SE Pyrenees. This is reflected by the light  $\delta^{18}\text{O}_{\text{fluid}}$  values between -4.5 and -3.6‰ VSMOW, the high  $^{87}\text{Sr}/^{86}\text{Sr}$  ratios between 0.708855 and 0.709747 and decreasing Y/Ho ratios from 52.87 to 38.31 measured in calcite vein fillings.
8. Secondary weld zones acted as preferential conduits for ascending hot Mg-rich fluids that partly dolomitized carbonates, whereas below the Upper Pedraforca basal thrust, Late Cretaceous seawater trapped within sediment pores, or evolved meteoric waters at ca. 70°C, migrated through fractures.



9. The comparison between the fluid evolution in the salt-related Upper Pedraforca thrust sheet and other diapiric areas hosting ore deposits suggests that meteoric percolation typically facilitates the development of supergene deposits during compressional tectonics. Additionally, fracturing of post-salt carbonate rocks in primary weld zones and evaporite detachments facilitates the transfer of basement-derived fluids from which ore mineralization could accumulate in fractures.

## ACKNOWLEDGEMENTS

This research was performed within the framework of DGICYT Spanish Project PGC2018-093903-B-C22 Ministerio de Ciencia, Innovación y Universidades/Agencia Estatal de Investigación/Fondo Europeo de Desarrollo Regional, Unión Europea, SUBTETIS (PIE-CSIC-201830E039), ALORBE (PIE-CSIC-202030E310) and Grup Consolidat de Recerca "Geologia Sedimentària" (2017SGR-824) and Generalitat de Catalunya, Grant/Award Number AGAUR 2017SGR-847. The isotopic analyses were carried out at "Centres Científics i Tecnològics" of the Universitat de Barcelona. Strontium analyses were done at the "CAI de Geocronología y Geoquímica Isotópica" of the Universidad Complutense de Madrid. The high resolution inductively coupled plasma-mass spectrometry analyses were carried out at labGEOTOP of the GEO3BCN-CSIC, a cofounded structure by FEDER-UE (Ref. CSIC08-4E-001). The clumped isotopes analyses were performed in the Qatar Stable Isotope Laboratory of Imperial College of London. E.G.R. acknowledges the Spanish Ministry of Science, Innovation and Universities for the "Ramón y Cajal" fellowship RYC2018-026335-I. We thank the accurate and constructive reviews from Richard Worden, Benoît Quesnel, an anonymous reviewer and the editor Kerry Gallagher, which greatly improved this manuscript.

## PEER REVIEW

The peer review history for this article is available at <https://publons.com/publon/10.1111/bre.12596>.


## DATA AVAILABILITY STATEMENT


The data that support the findings of this study are available from the corresponding author upon reasonable request.


## ORCID

David Cruset  <https://orcid.org/0000-0003-3683-5125>

Jaume Vergés  <https://orcid.org/0000-0002-4467-5291>

Enrique Gomez-Rivas  <https://orcid.org/0000-0002-1317-6289>

Irene Cantarero  <https://orcid.org/0000-0001-5744-6773>

Cédric M. John  <https://orcid.org/0000-0001-9711-1548>

Anna Travé  <https://orcid.org/0000-0002-2735-3733>

## REFERENCES

- Ábalos, B., Alonso, N., Berrocal, T., Furundarena, A., Gorospe, I., Martínez-Escauriaza, G., Matxain, I., & Sánchez-Lorda, M. E. (2003). Structural analysis of the Murguía diapir's peripheral troughs (Álava, Basque-Cantabrian Basin). *Geogaceta*, *34*, 7–10.
- Allen, P. A., & Allen, J. R. (2005). *Basin analysis: Principles and applications*. Blackwell.
- Allen, P. A., & Allen, J. R. (2013). *Basin analysis: Principles and application to petroleum play assessment* (3rd ed.). Wiley-Blackwell.
- Arnal, I., Calvet, F., Márquez, L., Márquez-Aliaga, A., & Porta, N. S. d. (2002). The epeiric carbonate platform (Imón and Isábena Formations) of the Upper Triassic from the Northeastern Iberian Peninsula. *Acta Geologica Hispanica*, *37*, 299–328.
- Aurell, M., Meléndez, G., & Olóriz, F. (2002). Jurassic. In W. Gibbons & T. Moreno (Eds.), *The geology of Spain* (pp. 221–254). The Geological Society of London.
- Banks, D. A., Davies, G. R., Yardley, B. W. D., McCaig, A. M., & Grant, N. T. (1991). The chemistry of brines from an Alpine thrust system in the Central Pyrenees: An application of fluid inclusion analysis to the study of fluid behavior in orogenesis. *Geochimica et Cosmochimica Acta*, *55*, 1021–1030.
- Bau, M., & Dulski, P. (1994). Evolution of the yttrium-holmium systematics of seawater through time. *Mineralogical Magazine*, *58*(A), 61–62.
- Bau, M., & Dulski, P. (1996). Distribution of yttrium and rare-earth elements in the Penge and Kuruman iron-formations, Transvaal Supergroup, South Africa. *Precambrian Research*, *79*, 37–55. [https://doi.org/10.1016/0301-9268\(95\)00087-9](https://doi.org/10.1016/0301-9268(95)00087-9)
- Beamud, E., Garcés, M., Cabrera, L., Muñoz, J. A., & Almar, Y. (2003). A new middle to late Eocene continental chronostratigraphy from NE Spain. *Earth and Planetary Science Letters*, *216*, 501–514. [https://doi.org/10.1016/S0012-821X\(03\)00539-9](https://doi.org/10.1016/S0012-821X(03)00539-9)
- Beaudoin, N., Huyghe, D., Bellahsen, N., Lacombe, O., Emmanuel, L., Mouthereau, F., & Ouahnon, L. (2015). Fluid systems and fracture development during syn-depositional fold growth: An example from the Pico del Aguila anticline, Sierras Exteriores, southern Pyrenees, Spain. *Journal of Structural Geology*, *70*, 23–38. <https://doi.org/10.1016/j.jsg.2014.11.003>
- Bickle, M. J., Wickham, S. M., Chapman, H. J., & Taylor, H. P. (1988). A strontium, neodymium and oxygen study of hydrothermal metamorphism and crustal anatexis in the Trois Seignerus Massif, Pyrenees, France. *Contributions to Mineralogy and Petrology*, *100*, 399–417.
- Bitzer, K., Travé, A., & Carmona, J. M. (2001). Fluid flow processes at basin scale. *Acta Geologica Hispanica*, *36*(1–2), 1–20.
- Bons, P. D., Elburg, M. A., & Gomez-Rivas, E. (2012). A review of the formation of tectonic veins and their microstructures. *Journal of Structural Geology*, *43*, 33–62. <https://doi.org/10.1016/j.jsg.2012.07.005>
- Bons, P. D., Fusswinkel, T., Gomez-Rivas, E., Markl, G., Wagner, T., & Walter, B. (2014). Fluid mixig from below in unconformity-related hydrothermal ore deposits. *Geology*, *42*(12), 1035–1038.
- Bouhrel, S., Leach, D. L., Johnson, C. A., Marsh, E., Salmi-Laouar, S., & Banks, D. A. (2016). A salt diapir-related Mississippi Valley-type deposit: The Bou Jaber Pb-Zn-Ba-F deposit, Tunisia: fluid inclusion and isotope study. *Mineralium Deposita*, *51*, 749–780.
- Boutoux, A., Verlaquet, A., Bellahsen, N., Lacombe, O., Villemant, B., Caron, B., Martin, E., Assayag, N., & Cartigny, P. (2014).

- Fluid systems above basement shear zones during inversion of pre-orogenic sedimentary basins (External Crystalline Massifs, Western Alps). *Lithos*, 206–207, 435–453. <https://doi.org/10.1016/j.lithos.2014.07.005>
- Burbank, D. W., Puigdefàbregas, C., & Muñoz, J. A. (1992). The chronology of the Eocene tectonic and stratigraphic development of the Eastern Pyrenean Foreland Basin. NE Spain. *Geological Society of America Bulletin*, 104, 1101–1120.
- Burbank, D. W., Vergés, J., Muñoz, J. A., & Benthams, P. (1992). Coeval inward- and forward-imbricating thrusting in the south-central Pyrenees, Spain: Timing and rates of shortening and deposition. *Geological Society of America Bulletin*, 104, 3–17.
- Burrell, L., & Teixell, A. (2021). Contractional salt tectonics and role of pre-existing diapiric structures in the Southern Pyrenean foreland fold-thrust belt (Montsec and Serres Marginals). *Journal of the Geological Society of London*, 178(4), jgs2020-085. <https://doi.org/10.1144/jgs2020-085>
- Caja, M. A., Permanyer, A., Marfil, R., Al-Asm, I. S., & Martín-Crespo, T. (2006). Fluid flow record from fracture-fill calcite in the Eocene limestones from the South-Pyrenean Basin (NE Spain) and its relationship to oil shows. *Journal of Geochemical Exploration*, 89, 27–32. <https://doi.org/10.1016/j.gexplo.2005.11.009>
- Calvet, F., Porta, N. S. d., & Salvany, J. M. (1993). Cronoestratigrafía (Palinología) del Triásico Sudpirenaico y del Pirineo Vasco-Cantábrico. *Acta Geologica Hispanica*, 28, 33–48.
- Canérot, J., Hudec, M. R., & Rockenbauch, K. (2005). Mesozoic diapirism in the Pyrenean orogen: Salt tectonics on a transform plate boundary. *AAPG Bulletin*, 89(2), 211–229. <https://doi.org/10.1306/09170404007>
- Cathelineau, M., Boiron, M. C., & Jakomulski, H. (2021). Triassic evaporites: A vast reservoir of brines mobilised successively during rifting and thrusting in the Pyrenees. *Journal of the Geological Society*, jgs2020-2259. <https://doi.org/10.1144/jgs2020-259>
- Cerling, T. E., & Quade, J. (1993). Stable carbon and oxygen isotopes in soil carbonates. In P. K. Swart, K. C. Lohman, J. Mckenzie, & S. Savin (Eds.), *Climate change in continental isotopic records* (pp. 217–231). American Geophysical Union.
- Choukroune, P., & ECORS Team. (1989). The ECORS Pyrenean deep seismic profile reflection data and the overall structure of an orogenic belt. *Tectonics*, 8, 23–39. <https://doi.org/10.1029/TC008i001p00023>
- Clerc, C., & Lagabrielle, Y. (2014). Thermal control on the modes of crustal thinning leading to mantle exhumation: Insights from the Cretaceous Pyrenean hot paleomargins. *Tectonics*, 33(7), 1340–1359. <https://doi.org/10.1002/2013TC003471>
- Clerc, C., Lagabrielle, Y., Labaume, P., Ringenbach, J. C., Vauchez, A., Nalpas, T., Bousquet, R., Ballard, J. F., Lahfid, A., & Fourcade, S. (2016). Basement – Cover decoupling and progressive exhumation of metamorphic sediments at hot rifted margin. Insights from the Northeastern Pyrenean analog. *Tectonophysics*, 686, 82–97. <https://doi.org/10.1016/j.tecto.2016.07.022>
- Cobbold, P. R., Diraison, M., & Rossello, E. A. (1999). Bitumen veins and Eocene transpression, Neuquén Basin, Argentina. *Tectonophysics*, 314, 423–442. [https://doi.org/10.1016/S0040-1951\(99\)00222-X](https://doi.org/10.1016/S0040-1951(99)00222-X)
- Coleman, A. J., Jackson, C. A. L., Duffy, O. B., & Nikolinakou, M. A. (2018). How, where, and when do radial faults grow near salt diapirs? *Geology*, 46(7), 655–658. <https://doi.org/10.1130/g40338.1>
- Cooper, M., & Warren, M. J. (2010). The geometric characteristics, genesis and petroleum significance of inversion structures. In R. D. Law, R. W. H. Butler, R. E. Holdsworth, M. Krabbendam, & R. A. Strachan (Eds.), *Continental tectonics and mountain building: The legacy of Peach and Horne* (Vol. 335, pp. 827–846). Geological Society, London, Special Publications.
- Costa, E., Garcés, M., López-Blanco, M., Beamud, E., Gómez-Paccard, M., & Larrasoana, J. C. (2010). Closing and continentalization of the South Pyrenean foreland basin (NE Spain): Magnetostratigraphical constraints. *Basin Research*, 22(6), 904–917. <https://doi.org/10.1111/j.1365-2117.2009.00452.x>
- Crognier, N., Hoareau, G., Aubourg, C., Dubois, M., Lacroix, B., Branellec, M., Callot, J. P., & Vennemann, T. (2018). Syn-orogenic fluid flow in the Jaca basin (south Pyrenean fold and thrust belt) from fracture and vein analyses. *Basin Research*, 30(2), 187–216. <https://doi.org/10.1111/bre.12249>
- Cruset, D., Cantarero, I., Benedicto, A., John, C. M., Vergés, J., Albert, R., Gerdes, A., & Travé, A. (2020). From hydroplastic to brittle deformation: Controls on fluid flow in fold and thrust belts. Insights from the Lower Pedraforca thrust sheet (SE Pyrenees). *Marine and Petroleum Geology*, 120, 104517. <https://doi.org/10.1016/j.marpetgeo.2020.104517>
- Cruset, D., Cantarero, I., Travé, A., Vergés, J., & John, C. M. (2016). Crestal graben fluid evolution during growth of the Puig-reig anticline (South Pyrenean fold and thrust belt). *Journal of Geodynamics*, 101, 30–50. <https://doi.org/10.1016/j.jog.2016.05.004>
- Cruset, D., Cantarero, I., Vergés, J., John, C. M., Muñoz-López, D., & Travé, A. (2018). Changes in fluid regime in syn-orogenic sediments during the growth of the south Pyrenean fold and thrust belt. *Global and Planetary Change*, 171, 207–224. <https://doi.org/10.1016/j.gloplacha.2017.11.001>
- Cruset, D., Vergés, J., Albert, R., Gerdes, A., Benedicto, A., Cantarero, I., & Travé, A. (2020). Quantifying deformation processes in the SE Pyrenees using U-Pb dating of fracture-filling calcites. *Journal of the Geological Society*, 177, 1186–1196. <https://doi.org/10.1144/jgs2020-014>
- Cruset, D., Vergés, J., Rodrigues, N., Belenguer, J., Pascual-Cebrian, E., Almar, Y., Pérez-Cáceres, I., Macchiavelli, C., Travé, A., Beranoaguirre, A., Albert, R., Gerdes, A., & Messenger, G. (2021). U-Pb dating of carbonate veins constraining timing of beef growth and oil generation within Vaca Muerta Formation and compression history in the Neuquén Basin along the Andean fold and thrust belt. *Marine and Petroleum Geology*, 132, 105204. <https://doi.org/10.1016/j.marpetgeo.2021.105204>
- Davison, I., Alsop, G. I., Evans, N. G., & Safaricz, M. (2000). Overburden deformation patterns and mechanisms of salt diapir penetration in the Central Graben, North Sea. *Marine and Petroleum Geology*, 17, 601–618. [https://doi.org/10.1016/S0264-8172\(00\)00011-8](https://doi.org/10.1016/S0264-8172(00)00011-8)
- Delvaux, D., & Sperner, B. (2003). New aspects of tectonic stress inversion with reference to the TENSOR program. In D. A. Nieuwland (Ed.), *New insights into structural interpretation and modelling* (Vol. 212, pp. 75–100). Geological Society, London, Special Publications.
- Deng, Y., Ren, J., Guo, Q., Cao, J., Wang, H., & Liu, C. (2017). Rare earth element geochemistry characteristics of seawater and porewater from deep sea in western Pacific. *Scientific Reports*, 7, 16539. <https://doi.org/10.1038/s41598-017-16379-1>
- Emery, D. (1987). Trace-element source and mobility during limestone burial diagenesis – An example from the Middle



- Jurassic of eastern England. *Geological Society, London, Special Publications*, 36(1), 201–217. <https://doi.org/10.1144/gsl.sp.1987.036.01.16>
- Fernández, M., Marzán, I., Correia, A., & Ramalho, E. (1998). Heat flow, heat production, and lithospheric thermal regime in the Iberian Peninsula. *Tectonophysics*, 291, 29–53. [https://doi.org/10.1016/S0040-1951\(98\)00029-8](https://doi.org/10.1016/S0040-1951(98)00029-8)
- Ferrer, O., Jackson, M. P. A., Roca, E., & Rubinat, M. (2012). Evolution of salt structures during extension and inversion of the Offshore Parentis Basin (Eastern Bay of Biscay). In G. I. Alsop, S. G. Archer, A. J. Hartley, N. T. Grant, & R. Hodgkinson (Eds.), *Salt tectonics, sediments and prospectivity* (Vol. 363, pp. 361–379). Geological Society, London, Special Publications.
- Fillon, C., Huismans, R. S., van der Beek, P., & Muñoz, J. A. (2013). Syntectonic sedimentation controls on the evolution of the southern Pyrenean fold-and-thrust belt: Inferences from coupled tectonic-surface processes models. *Journal of Geophysical Research*, 118, 5665–5680. <https://doi.org/10.1002/jgrb.50368>
- Fischer, M. P., Higuera-Díaz, I. C., Evans, M. A., Perry, E. C., & Leticariu, L. (2009). Fracture-controlled paleohydrology in a map-scale detachment fold: Insights from the analysis of fluid inclusions in calcite and quartz veins. *Journal of Structural Geology*, 31(12), 1490–1510. <https://doi.org/10.1016/j.jsg.2009.09.004>
- Fischer, M. P., Kenroy, P. R., & Smith, A. P. (2013, May 19–22). *Fluid systems around salt diapirs*. Paper presented at the AAPG Annual Convention and Exhibition, Pittsburgh, Pennsylvania.
- Fontana, S., Nader, F. H., Morad, S., Ceriani, A., Al-Aasm, I. S., Daniel, J.-M., & Mengus, J.-M. (2014). Fluid–rock interactions associated with regional tectonics and basin evolution. *Sedimentology*, 61(3), 660–690. <https://doi.org/10.1111/sed.12073>
- Ford, M., & Vergés, J. (2021). Evolution of a salt-rich transtensional rifted margin, eastern North Pyrenees, France. *Journal of the Geological Society*, 178(1), jgs2019-2157. <https://doi.org/10.1144/jgs2019-157>
- García-Senz. (2002). *Cuencas extensivas del Cretácico Inferior en los Pirineos centrales. Formación y subsecuente inversión* [PhD thesis]. Universitat de Barcelona, Spain.
- Garnit, H., Boni, M., Buongiovanni, G., Arfè, G., Mondillo, N., Joachimski, M., Bouhrel, S., & Balassone, G. (2018). C-O stable isotopes geochemistry of Tunisian Nonsulfide Zinc deposits: A first look. *Minerals*, 8, 13.
- Godeau, N., Deschamps, P., Guihou, A., Leonide, P., Tendill, A., Gerdes, A., Hamelin, B., & Girard, J. P. (2018). U-Pb dating of calcite cement and diagenetic history in microporous carbonate reservoirs: Case of the Urgonian Limestone, France. *Geology*, 46, 247–250. <https://doi.org/10.1130/G39905.1>
- Gomez-Rivas, E., Bons, P. D., Koehn, D., Urai, J. L., Arndt, M., Virgo, S., Laurich, B., Zeeb, C., Stark, L., & Blum, P. (2014). The Jabal Akhdar dome in the Oman mountains: Evolution of a dynamic fracture system. *American Journal of Science*, 314, 1104–1139. <https://doi.org/10.2475/07.2014.02>
- Gomez-Rivas, E., Corbella, M., Martín-Martín, J. D., Stafford, S. L., Teixell, A., Bons, P. D., Griera, A., & Cardellach, E. (2014). Reactivity of dolomitizing fluids and Mg source evaluation of fault-controlled dolomitization at the Benicàssim outcrop analogue (Maestrat basin, E Spain). *Marine and Petroleum Geology*, 55, 26–42. <https://doi.org/10.1016/j.marpetgeo.2013.12.015>
- Gregg, J. M., & Sibley, D. F. (1984). Epigenetic dolomitization and the origin of xenotopic dolomite texture. *Journal of Sedimentary Petrology*, 54, 908–931.
- Grool, A. R., Ford, M., Vergés, J., Huismans, R. S., Christophoul, F., & Dielforder, A. (2018). Insights into the crustal-scale dynamics of a doubly Vergent Orogen from a quantitative analysis of its forelands: A case study of the Eastern Pyrenees. *Tectonics*, 37(2), 450–476. <https://doi.org/10.1002/2017TC004731>
- Hansman, R. J., Albert, R., Gerdes, A., & Ring, U. (2018). Absolute ages of multiple generations of brittle structures by U-Pb dating of calcite. *Geology*, 46(3), 207–210. <https://doi.org/10.1130/G39822.1>
- Hassanlouei, B. T., & Rajabzadeh, M. A. (2019). Iron ore deposits associated with Hormuz evaporitic series in Hormuz and Pohl salt diapirs, Hormuzgan province, southern Iran. *Journal of Asian Earth Sciences*, 172, 30–55. <https://doi.org/10.1016/j.jseaes.2018.08.024>
- Hausegger, S., Kurz, W., Rabitsch, R., Kiechl, E., & Brosch, F.-J. (2010). Analysis of the internal structure of a carbonate damage zone: Implications for the mechanisms of fault breccia formation and fluid flow. *Journal of Structural Geology*, 32(9), 1349–1362. <https://doi.org/10.1016/j.jsg.2009.04.014>
- Hoareau, G., Crognier, N., Lacroix, B., Aubourg, C., Roberts, N. M. W., Niemi, N., Branell, M., Beaudoin, N., & Ruiz, I. S. (2021). Combination of 47 and U-Pb dating in tectonic calcite veins unravel the last pulses related to the Pyrenean Shortening (Spain). *Earth and Planetary Science Letters*, 553, 116636.
- Hudec, M. R., Dooley, T. P., Burrell, L., Teixell, A., & Fernandez, N. (2021). An alternative model for the role of salt depositional configuration and preexisting salt structures in the evolution of the Southern Pyrenees, Spain. *Journal of Structural Geology*, 146, 104325. <https://doi.org/10.1016/j.jsg.2021.104325>
- Immenhauser, A., Dublyansky, Y. V., Verwer, K., Fleitman, D., & Pashenko, S. E. (2007). Textural, elemental and isotopic characteristics of Pleistocene phreatic cave deposits (Jabal Madar, Oman). *Journal of Sedimentary Research*, 77(1–2), 68–88. <https://doi.org/10.2110/jsr.2007.012>
- Incerpi, N., Martire, L., Manatschal, G., & Bernasconi, S. M. (2017). Evidence of hydrothermal fluid flow in a hyperextended rifted margin: The case study of the Err nappe (SE Switzerland). *Swiss Journal of Geosciences*, 110, 439–456. <https://doi.org/10.1007/s00015-016-0235-2>
- Incerpi, N., Martire, L., Manatschal, G., Bernasconi, S. M., Gerdes, A., Czuppon, G., Palcsu, L., Karner, G. D., Johnson, C. A., & Figueredo, F. (2020). Hydrothermal fluid flow associated to the extensional evolution of the Adriatic rifted margin: Insights from the pre- to post-rift sedimentary sequence (SE Switzerland, N ITALY). *Basin Research*, 32(1), 91–115. <https://doi.org/10.1111/bre.12370>
- Izquierdo-Llavall, E., Menant, A., Aubourg, C., Callot, J. P., Hoareau, G., Camps, P., Péré, E., & Lahfid, A. (2020). Preorogenic folds and Syn-Orogenic basement tilts in an inverted hyperextended margin: The Northern Pyrenees case study. *Tectonics*, 39, e2019TC005719. <https://doi.org/10.1029/2019TC005719>
- Jolivet, M., & Boulvais, P. (2021). Global significance of oxygen and carbon isotope compositions of pedogenic carbonates since the Cretaceous. *Geoscience Frontiers*, 12(4), 101132. <https://doi.org/10.1016/j.gsf.2020.12.012>
- Labaume, P., Meresse, F., Joliver, M., Teixell, A., & Lahfid, A. (2016). Tectonothermal history of an exhumed thrust-sheet-top basin: An example from the south Pyrenean thrust belt. *Tectonics*, 35, 1280–1313. <https://doi.org/10.1002/2016TC004192>
- Labaume, P., & Teixell, A. (2020). Evolution of salt structures of the Pyrenean rift (Chaînons Béarnais, France): From

- hyper-extension to tectonic inversion. *Tectonophysics*, 785, 228451. <https://doi.org/10.1016/j.tecto.2020.228451>
- Lacroix, B., Baumgartner, L. P., Bouvier, A. S., Kempton, P. D., & Vennemann, T. (2018). Multi fluid-flow record during episodic mode I opening: Amicrostructural and SIMS study (Cotiella Thrust Fault, Pyrenees). *Earth and Planetary Science Letters*, 503, 37–46. <https://doi.org/10.1016/j.epsl.2018.09.016>
- Lacroix, B., Travé, A., Buatier, M., Labaume, P., Vennemann, T., & Dubois, M. (2014). Syntectonic fluid-flow along thrust faults: Example of the South-Pyrenean fold-and-thrust belt. *Marine and Petroleum Geology*, 49, 84–98. <https://doi.org/10.1016/j.marpetgeo.2013.09.005>
- Lagabriele, Y., Labaume, P., & de Saint Blanquat, M. (2010). Mantle exhumation, crustal denudation, and gravity tectonics during Cretaceous rifting in the Pyrenean realm (SW Europe): Insights from the geological setting of the lherzolite bodies. *Tectonics*, 29(4), TC4012. <https://doi.org/10.1029/2009TC002588>
- Lawrence, M. G., Creig, A., Collerson, K. D., & Kamber, B. S. (2006). Rare earth element and yttrium variability in south east Queensland Waterways. *Aquatic Geochemistry*, 12, 39–72. <https://doi.org/10.1007/s10498-005-4471-8>
- Lécuyer, C., Reynard, B., & Grandjean, P. (2004). Rare earth element evolution of Phanerozoic seawater recorded in biogenic apatites. *Chemical Geology*, 204(1–2), 63–102. <https://doi.org/10.1016/j.chemgeo.2003.11.003>
- Lescoutre, R., Tugend, J., Brune, S., Masini, E., & Manatschal, G. (2019). Thermal evolution of asymmetric hyperextended magma-poor rift systems: Results from numerical modeling and Pyrenean field observations. *Geochemistry, Geophysics, Geosystems*, 20, 4567–4587.
- López-Mir, B., Muñoz, J. A., & García-Senz, J. (2015). Extensional salt tectonics in the partially inverted Cotiella post-rift basin (south-central Pyrenees): Structure and evolution. *International Journal of Earth Sciences*, 104(2), 419–434. <https://doi.org/10.1007/s00531-014-1091-9>
- Lynch, G., Keller, J. V. A., & Giles, P. S. (1998). Influence of the ainslie detachment on the stratigraphy of the Maritimes basin and mineralization in the Windsor Group of Northern Nova Scotia, Canada. *Economic Geology*, 93, 703–718.
- Machel, H. G. (2004). Concepts and models of dolomitization: A critical reappraisal. *Geological Society, London, Special Publications*, 235(1), 7–63.
- Mangenot, X., Gasparrini, M., Rouchon, V., & Bonifacie, M. (2018). Basin-scale thermal and fluid flow histories revealed by carbonate clumped isotopes ( $\Delta 47$ ) – Middle Jurassic carbonates of the Paris Basin depocentre. *Sedimentology*, 65(1), 123–150. <https://doi.org/10.1111/sed.12427>
- Martín-Chivelet, J. (2002). Cretaceous. In W. Gibbons & T. Moreno (Eds.), *The geology of Spain* (pp. 264–292). The Geological Society of London.
- Martínez, A., Berástegui, X., Losantos, M., & Schöllhorn, E. (2001). Estructura de los mantos superior e inferior del Pedraforca (Pirineos orientales). *Geogaceta*, 30, 183–186.
- Masoumi, S., Reuning, L., Back, S., Sandrin, A., & Kukla, P. A. (2014). Buried pockmarks on the Top Chalk surface of the Danish North Sea and their potential significance for interpreting palaeocirculation patterns. *International Journal of Earth Sciences*, 103, 563–578. <https://doi.org/10.1007/s00531-013-0977-2>
- Mató, E., Saula, E., Martínez-Rius, A., Muñoz, J. A., & Escuer, J. (1994). Memoria de la Hoja nº 293 (Berga). *Mapa Geológico de España E. 1:50.000 (MAGNA), Segunda Serie, Primera Edición. IGME*, 66.
- McArthur, J. M., Howarth, R. J., & Bailey, T. R. (2001). Strontium isotope stratigraphy: LOWESS Version 3: Best fit to the Marine Sr-Isotope curve for 0–509 Ma and accompanying look-up table for deriving numerical age. *Journal of Geology*, 109, 155–170. <https://doi.org/10.1086/319243>
- McCaig, A. M., Wayne, D. M., Marshall, J. D., Banks, D., & Henderson, I. (1995). Isotopic and fluid inclusion studies of fluid movement along the Gavarnie Thrust, central Pyrenees: Reaction fronts in carbonate mylonites. *American Journal of Science*, 295, 309–343. <https://doi.org/10.2475/ajs.295.3.309>
- McLennan, S. (1989). Rare earth elements in sedimentary rocks; influence of provenance and sedimentary processes. *Reviews in Mineralogy and Geochemistry*, 21, 277–290.
- Mencos, J., Carrera, N., & Muñoz, J. A. (2015). Influence of rift basin geometry on the subsequent postrift sedimentation and basin inversion: The Organyà Basin and the Bóixols thrust sheet (south central Pyrenees). *Tectonics*, 34, 1452–1474. <https://doi.org/10.1002/2014TC003692>
- Metcalfe, J. R., Fitzgerald, P. G., Baldwin, S. L., & Muñoz, J. A. (2009). Thermochronology of a convergent orogen: Constraints on the timing of thrust faulting and subsequent exhumation of the Maladeta Pluton in the Central Pyrenean Axial Zone. *Earth and Planetary Science Letters*, 287, 488–503. <https://doi.org/10.1016/j.epsl.2009.08.036>
- Mey, P. H. W., Nagtegaal, P. J. C., Roberti, K. J., & Hartevelt, J. J. A. (1968). Lithostratigraphic subdivision of post-Hercinian deposits in the south-central Pyrenees, Spain. *Leidse Geologische Mededelingen*, 41, 21–228.
- Moragas, M., Baqués, V., Travé, A., Martín-Martín, J. D., Saura, E., Messenger, G., Hunt, D., & Vergés, J. (2020). Diagenetic evolution of lower Jurassic platform carbonates flanking the Tazoult salt wall (Central High Atlas, Morocco). *Basin Research*, 32(3), 546–566. <https://doi.org/10.1111/bre.12382>
- Motte, G., Hoareau, G., Callot, J. P., Révillon, S., Piccoli, F., Calassou, S., & Gaucher, E. C. (2021). Rift and salt-related multi-phase dolomitization: Example from the northwestern Pyrenees. *Marine and Petroleum Geology*, 126, 104932. <https://doi.org/10.1016/j.marpetgeo.2021.104932>
- Mouttaqi, A., Rjimat, E. C., Maacha, A., Michard, A., & Soulaïmani, A. (2011). Les principales mines du Maroc. In A. Michard, O. Saddiqi, A. Chalouan, E. C. Rjimat, & A. Mouttaqi (Eds.), *New geological and mining guidebooks of Morocco*. Service géologique du Maroc.
- Muñoz, J. A. (1992). Evolution of a continental collision belt: ECORS–Pyrenees crustal balanced section. In K. R. McClay (Ed.), *Thrust tectonics* (pp. 235–246). Chapman & Hall.
- Muñoz, J. A. (2002). The Pyrenees. In W. Gibbons & T. Moreno (Eds.), *The geology of Spain* (pp. 370–385). Geological Society.
- Muñoz, J. A., Vergés, J., Martínez, A., Fleta, J., Cirés, J., Casas, J. M., & Sàbat, F. (1994). Mapa geológico de la Hoja nº 256 (Ripoll). *Mapa Geológico de España E. 1:50.000. Segunda Serie (MAGNA), Primera edición. IGME*.
- Muñoz-López, D., Alías, G., Cruset, D., Cantarero, I., Jonh, C. M., & Travé, A. (2020). Influence of basement rocks on fluid evolution during multiphase deformation: The example of the Estamariu thrust in the Pyrenean Axial Zone. *Solid Earth Discuss*, 2020, 1–39. <https://doi.org/10.5194/se-2020-65>



- Muñoz-López, D., Cruset, D., Cantarero, I., Benedicto, A., John, C. M., & Travé, A. (2020). Fluid dynamics in a thrust fault inferred from petrology and geochemistry of calcite veins: An example from the Southern Pyrenees. *Geofluids*, 2020, 8815729. <https://doi.org/10.1155/2020/8815729>
- Nardini, N., Muñoz-López, D., Cruset, D., Cantarero, I., Martín-Martín, J. D., Benedicto, A., Gomez-Rivas, E., John, C. M., & Travé, A. (2019). From early contraction to post-folding fluid evolution in the frontal part of the Bóixols thrust sheet (southern Pyrenees) as revealed by the texture and geochemistry of calcite cements. *Minerals*, 9(2), 117. <https://doi.org/10.3390/min9020117>
- N'Diaye, I., Essaifi, A., Dubois, N., Lacroix, B., Goodenough, K. M., & Maacha, L. (2016). Fluid flow and polymetallic sulfide mineralization in the Kettara shear zone (Jebilet Massif, Variscan Belt, Morocco). *Journal of African Earth Sciences*, 119, 17–37. <https://doi.org/10.1016/j.jafrearsci.2016.03.010>
- Pagel, M., Bonifacie, M., Schneider, D. A., Gautheron, C., Brigaud, B., Calmels, D., Cros, A., Saint-Bezar, B., Landrein, P., Sutcliffe, C., Davis, D., & Chaduteau, C. (2018). Improving paleohydrological and diagenetic reconstructions in calcite veins and breccia of a sedimentary basin by combining  $\Delta 47$  temperature,  $\delta 18\text{O}$  water and U-Pb age. *Chemical Geology*, 481, 1–17. <https://doi.org/10.1016/j.chemgeo.2017.12.026>
- Perona, J., Canals, A., & Cardellach, E. (2018). Zn-Pb mineralization associated with salt diapirs in the Basque-Cantabrian Basin, Northern Spain: Geology, geochemistry, and genetic model. *Economic Geology*, 113(5), 1133–1159. <https://doi.org/10.5382/econgeo.2018.4584>
- Peybernès, B. (1976). *Le Jurassique et le Crétacé inférieur des Pyrénées franco-espagnoles entre la Garonne et le Méditerranée* [PhD thesis], Université de Toulouse, Toulouse, France.
- Pi, M. E., Samsó-Escola, J. M., Vilella, L., Arbués, P., Casanovas, J., & Berastegui, X. (2001). Mapa geológico de la Hoja nº 291 (Oliana). *Mapa Geológico de España E. 1:50.000. Segunda Serie (MAGNA), Primera edición. IGME*.
- Puigdefàbregas, C., & Souquet, P. (1986). Tecto-sedimentary cycles and deposition sequences of the Mesozoic and Tertiary from the Pyrenees. *Tectonophysics*, 129, 173–203.
- Rahl, J. M., Haines, S. H., & van der Pluijm, B. A. (2011). Links between orogenic wedge deformation and erosional exhumation: Evidence from illite age analysis of fault rock and detrital thermochronology of syn-tectonic conglomerates in the Spanish Pyrenees. *Earth and Planetary Science Letters*, 307(1–2), 180–190. <https://doi.org/10.1016/j.epsl.2011.04.036>
- Reuning, L., Schoenherr, J., Heinmann, A., Urai, J. L., Littke, R., Kukla, P. A., & Rawahi, Z. (2009). Constraints on the diagenesis, stratigraphy and internal dynamics of the surface-piercing salt domes in the Ghaba Salt Basin (Oman): A comparison to the Ara Group in the South Oman Salt Basin. *GeoArabia*, 14(3), 83–120.
- Rodrigues, N., Cobbold, P. R., Loseth, H., & Ruffet, G. (2009). Widespread bedding-parallel veins of fibrous calcite ('beef') in a mature source rock (Vaca Muerta Fm, Neuquén Basin, Argentina): Evidence for overpressure and horizontal compression. *Journal of the Geological Society*, 166, 695–709. <https://doi.org/10.1144/0016-76492008-111>
- Roure, F., Choukroune, P., Berastegui, J., Muñoz, J. A., Villien, A., Matheron, P., Bareyt, M., Seguret, M., Camara, P., & Deramond, J. (1989). Ecoreep seismic data and balanced cross sections: Geometric constraints on the evolution of the Pyrenees. *Tectonics*, 8(1), 41–50. <https://doi.org/10.1029/TC008i001p00041>
- Roure, F., Swennen, R., Schneider, F., Faure, J. L., Ferket, H., Guilhaumou, N., Osadetz, K., Robion, P., & Vandeginste, V. (2005). Incidence and importance of tectonics and natural fluid migration on reservoir evolution in foreland fold-and-thrust belts. *Oil & Gas Science and Technology*, 60(1), 67–106. <https://doi.org/10.2516/ogst:2005006>
- Rouvier, H., Perthuisot, V., & Mansouri, A. (1985). Pb-Zn deposits and salt-bearing diapirs in Southern Europe and North Africa. *Economic Geology*, 80, 666–687. <https://doi.org/10.2113/gsecongeo.80.3.666>
- Salardon, R., Carpentier, C., Bellahsen, N., Pironon, J., & France-Lanord, C. (2017). Interactions between tectonics and fluid circulations in an inverted hyper-extended basin: Example of mesozoic carbonate rocks of the western North Pyrenean Zone (Chaînons Béarnais, France). *Marine and Petroleum Geology*, 80, 563–586. <https://doi.org/10.1016/j.marpetgeo.2016.11.018>
- Sans, M. (2003). From thrust tectonics to diapirism. The role of evaporites in the kinematic evolution of the eastern South Pyrenean front. *Geologica Acta*, 1(3), 239–259.
- Saura, E., Ardèvol, L. L., Teixell, A., & Vergés, J. (2016). Rising and falling diapirs, shifting depocenters, and flap overturning in the Cretaceous Sopeira and Sant Gervàs subbasins (Ribagorça Basin, southern Pyrenees). *Tectonics*, 35(3), 638–662. <https://doi.org/10.1002/2015TC004001>
- Séguret, M. (1972). *Étude tectonique des nappes et séries décollées de la partie centrale du versant sud des Pyrénées*: Pub. USTELA, sér. Geol. Struct. n.2, Montpellier.
- Serra-Kiel, J., Mató, E., Saula, E., Travé, A., Ferràndez-Cañadell, C., Àlvarez-Pérez, G., Franquès, J., & Romero, J. (2003). An inventory of the marine and transitional middle/upper Eocene deposits of the Southeastern Pyrenean Foreland Basin (NE Spain). *Geologica Acta*, 1(2), 201–229.
- Serra-Kiel, J., Travé, A., Mató, E., Saula, E., Ferràndez-Cañadell, C., Busquets, P., Tosquella, J., & Vergés, J. (2003). Marine and transitional middle/upper Eocene units of the Southeastern Pyrenean Foreland Basin (NE Spain). *Geologica Acta*, 1(2), 177–200.
- Serrano, A., & Martínez del Olmo, W. (1990). Tectónica salina en el Dominio Cantabro-Navarro: Evolución, edad y origen de las estructuras salinas. In F. Ortí & J. M. Salvany (Eds.), *Formaciones evaporíticas de la Cuenca del Ebro y cadenas periféricas, y de la zona de Levante* (pp. 39–53). Enresa.
- Sharp, I., Gillespie, P., Morsalnezhad, D., Taberner, C., Karpuz, R., Vergés, J., Horbury, A., Pickard, N., Garland, J., & Hunt, D. (2010). Stratigraphic architecture and fracture-controlled dolomitization of the Cretaceous Khami and Bangestan groups: An outcrop case study, Zagros Mountains, Iran. In F. S. P. V. Buchem, K. D. Gerdes, & M. Esteban (Eds.), *Mesozoic and cenozoic carbonate systems of the mediterranean and the middle east: Stratigraphic and diagenetic reference models* (Vol. 329, pp. 343–396). Geological Society, London, Special Publications.
- Sheppard, S. M. F., Charef, A., & Bouhleb, S. (1996). Diapirs and Zn-Pb mineralization: A general model based on Tunisian (N. Africa) and Gulf Coast (U.S.A.) deposits. In D. F. Sangster (Ed.), *Carbonate-hosted lead-zinc deposits: 75th anniversary volume* (Vol. 4, pp. 230–243). Society of Economic Geology. <https://doi.org/10.5382/SP.04>
- Sibley, D. F., & Gregg, J. M. (1987). Classification of dolomite rock textures. *Journal of Sedimentary Petrology*, 57, 967–975.
- Sijing, H., Keke, H., Jie, L., & Yefang, L. (2014). The relationship between dolomite textures and their formation temperature: A case study from the Permian-Triassic of the Sichuan Basin and

- the Lower Paleozoic of the Tarim Basin. *Petroleum Science*, 11, 39–51. <https://doi.org/10.1007/s12182-014-0316-7>
- Skelton, P. W., Gili, E., Vicens, E., Obrador, A., & López, G. (2003). Revised lithostratigraphy of the Upper Cretaceous (Santonian) carbonate platform succession on the northern flank of Sant Corneli, southern Central Pyrenees. *Journal of Iberian Geology*, 29, 73–87.
- Smith, A. P., Fischer, M. P., & Evans, M. A. (2012). Fracture-controlled palaeohydrology of a secondary salt weld, La Popa Basin, NE Mexico. *Geological Society, London, Special Publications*, 363(1), 107–130. <https://doi.org/10.1144/sp363.6>
- Stackelberg, U. (1960). Der diapir von Murgía (Nordspanien). *Beiheft zum Geologischen Jahrbuch*, 66, 63–94.
- Taylor, B. E. (1987). Stable isotope geochemistry of ore-forming fluids. In T. K. Kyser (Ed.), *Short course in stable isotope geochemistry of low temperature fluids* (Vol. 13, pp. 337–418). Mineral Association of Canada.
- Tostevin, R., Shields, G. A., Tarbuck, G. M., He, T., Clarckson, M. O., & Wood, R. A. (2016). Effective use of cerium anomalies as a redox proxy in carbonate-dominated marine settings. *Chemical Geology*, 438, 146–162. <https://doi.org/10.1016/j.chemgeo.2016.06.027>
- Travé, A., Labaume, P., Calvet, F., & Soler, A. (1997). Sediment dewatering and pore fluid migration along thrust faults in a foreland basin inferred from isotopic and elemental geochemical analyses (Eocene southern Pyrenees, Spain). *Tectonophysics*, 282(1–4), 375–398. [https://doi.org/10.1016/S0040-1951\(97\)00225-4](https://doi.org/10.1016/S0040-1951(97)00225-4)
- Travé, A., Labaume, P., & Vergés, J. (2007). Fluid systems in foreland fold and thrust belts: An overview from the Southern Pyrenees. In O. Lacombe, J. Lavé, F. Roure, & J. Vergés (Eds.), *Thrust belts and foreland basins: From fold kinematics to hydrocarbon systems* (pp. 93–115). Springer.
- Trincal, V., Buatier, M., Charpentier, D., Lacroix, B., Lanari, P., Labaume, P., Lahfid, A., & Venneman, T. (2017). Fluid–rock interactions related to metamorphic reducing fluid flow in meta-sediments: Example of the Pic-de-Port-Vieux thrust (Pyrenees, Spain). *Contributions to Mineralogy and Petrology*, 172, 78. <https://doi.org/10.1007/s00410-017-1394-5>
- Ullastre, J., & Masriera, A. (2004). PEDRAFORCA: Estratigrafia y estructura (Pirineo catalán, España). *Treballs del Museu de Geologia de Barcelona*, 12, 11–52.
- Van Geet, M., Swennen, R., Durmishi, C., Roure, F., & Muecher, P. (2002). Paragenesis of Cretaceous to Eocene carbonate reservoirs in the Ionian fold and thrust belt (Albania): Relation between tectonism and fluid flow. *Sedimentology*, 49, 697–718.
- Veizer, J., Ala, D., Azmy, K., Bruckschen, P., Buhl, D., Bruhn, F., Carden, G. A. F., Diener, A., Ebner, S., Godderis, Y., Jasper, T., Korte, C., Pawellek, F., Podlaha, O. G., & Strauss, H. (1999).  $^{87}\text{Sr}/^{86}\text{Sr}$ ,  $\delta^{13}\text{C}$  and  $\delta^{18}\text{O}$  evolution of Phanerozoic seawater. *Chemical Geology*, 161, 59–88.
- Veizer, J., & Hoefs, J. (1976). Nature of O18/O16 and C13/C12 secular trends in sedimentary carbonate rocks. *Geochimica et Cosmochimica Acta*, 40, 1387–1395.
- Vergés, J. (1993). *Estudi geològic del vessant sud del Pirineu oriental i central. Evolució cinemàtica en 3D* (pp. 1–199) [PhD thesis]. University of Barcelona.
- Vergés, J., Fernández, M., & Martínez, A. (2002). The Pyrenean orogen: pre-, syn-, and post-collisional evolution. In G. Rosenbaum & G. Lister (Eds.), *Reconstruction of the evolution of the Alpine-Himalayan Orogen*. *Journal of the Virtual Explorer*, 8, 55–74.
- Vergés, J., & Garcia-Senz, J. (2001). Mesozoic evolution and Cainozoic inversion of the Pyrenean Rift. In P. A. Ziegler, W. Cavazza, A. H. F. Robertson, & S. Crasquin-Soleau (Eds.), *Peri-Tethys Memoir 6: Peri-Tethyan Rift/Wrench Basins and Passive Margins* (Vol. 186, pp. 187–212). Mémoires du Muséum National d'Histoire Naturelle, Paris.
- Vergés, J., Kullberg, J. C., Casas-Sainz, A., de Vicente, G., Duarte, L. V., Fernández, M., Gómez, J. J., Gómez-Pugnaire, M. T., Jabaloy-Sánchez, A., López-Gómez, J., Macchiavelli, C., Martín-Algarra, A., Martín-Chivelet, J., Muñoz, J. A., Quesada, C., Terrinha, P., Torné, M., & Vegas, R. (2019). An introduction to the Alpine Cycle in Iberia. In C. Quesada & J. T. Oliveira (Eds.), *The geology of Iberia: A geodynamic approach: Volume 3: The Alpine cycle* (pp. 1–14). Springer International.
- Vergés, J., Martínez, A., Domingo, F., Muñoz, J. A., Losantos, M., Fleta, J., & Gisbert, J. (1994). Mapa geológico de la Hoja nº 255 (La Pobra de Lillet). *Mapa Geológico de España E. 1:50.000. Segunda Serie (MAGNA), Primera edición. IGME*.
- Vergés, J., Martínez, A., & Muñoz, J. A. (1992). South Pyrenean fold and thrust belt: The role of foreland evaporitic levels in thrust geometry. In K. McClay (Ed.), *Thrust tectonics* (pp. 255–264). Chapman & Hall.
- Vicente, A., Martín-Closas, C., Arz, J. A., & Oms, O. (2015). Mastrichtian-basal Paleocene charophyte biozonation and its calibration to the Global Polarity Time Scale in the southern Pyrenees (Catalonia, Spain). *Cretaceous Research*, 52, 268–285. <https://doi.org/10.1016/j.cretres.2014.10.004>
- Warren, J. (2000). Dolomite: Occurrence, evolution and economically important associations. *Earth-Science Reviews*, 52(1–3), 1–81. [https://doi.org/10.1016/S0012-8252\(00\)00022-2](https://doi.org/10.1016/S0012-8252(00)00022-2)
- Webb, G. E., & Kamber, B. S. (2000). Rare earth elements in Holocene reefal microbialites: A new shallow seawater proxy. *Geochimica et Cosmochimica Acta*, 64(9), 1557–1565. [https://doi.org/10.1016/S0016-7037\(99\)00400-7](https://doi.org/10.1016/S0016-7037(99)00400-7)
- Weger, R. J., Murray, S. T., McNeill, D. F., Swart, P. K., Eberli, G. P., Rodríguez-Blanco, L., Tenaglia, M., & Rueda, L. E. (2019). Paleothermometry and distribution of calcite beef in the Vaca Muerta Formation, Neuquén Basin, Argentina. *AAPG Bulletin*, 103(4), 931–950. <https://doi.org/10.1306/10021817384>
- Zhao, L., Chen, Z. Q., Algeo, T. J., Chen, J., Chen, Y., Tong, J., Gao, S., Zhou, L., Hu, Z., & Liu, Y. (2013). Rare-earth element patterns in conodont albid crowns: Evidence for massive inputs of volcanic ash during the latest Permian biocrisis? *Global and Planetary Change*, 105, 135–151. <https://doi.org/10.1016/j.gloplacha.2012.09.001>

## SUPPORTING INFORMATION

Additional supporting information may be found online in the Supporting Information section.

**How to cite this article:** Cruset, D., Vergés, J., Benedicto, A., Gomez-Rivas, E., Cantarero, I., John, C. M., & Travé, A. (2021). Multiple fluid flow events from salt-related rifting to basin inversion (Upper Pedraforca thrust sheet, SE Pyrenees). *Basin Research*, 33, 3102–3136. <https://doi.org/10.1111/bre.12596>